

GOTO identification and broadband modelling of the counterpart to the SVOM GRB 250818B

S. Belkin,¹  G. P. Lamb,² K. Ackley,³ M. E. Wortley,^{4,5} S. McGee,^{4,5} G. Schroeder,⁶ M. Shrestha,¹ B. P. Gompertz,^{4,5} D. K. Galloway,¹ R. Starling,⁷ W.-f. Fong,^{8,9} T. Laskar,⁸ C. Liu,^{8,9} A. C. Gordon,^{8,9} N. Pankov,^{10,11} A. E. Volvach,¹² L. N. Volvach,¹² A. Shein,¹³ A. Pozanenko,^{10,11} M. J. Dyer,^{14,15} J. Lyman,³ K. Ulaczyk,³ D. Steeghs,³ V. S. Dhillon,^{14,16} P. O'Brien,⁷ G. Ramsay,¹⁷ K. Noysena,¹⁸ R. Kotak,¹⁹ R. P. Breton,²⁰ L. K. Nuttall,²¹ D. Pollacco,³ S. Awiphan,¹⁸ J. Casares,^{16,22} P. Chote,³ A. Chrimes,²³ R. Eyles-Ferris,⁷ B. Godson,³ P. Irawati,¹⁸ D. Jarvis,¹⁴ Y. Julakanti,⁷ L. Kelsey,²⁴ M. R. Kennedy,²⁵ T. Killestein,³ A. Kumar,³ A. Levan,²³ S. Littlefair,¹⁴ M. Magee,³ S. Mandhai,²⁰ D. Mata Sánchez,^{16,22} S. Mattila,^{19,26} J. McCormac,³ D. Mkrtichian,¹⁸ S. Moran,⁷ J. Mullaney,¹⁴ D. O'Neill,³ M. Patel,⁷ K. Pu,¹ M. Pursiainen,³ A. Sahu,³ U. Sawangwit,¹⁸ E. Stanway,³ Y. Sun,⁷ B. Warwick,³ and K. Wiersema²⁷

Affiliations are listed at the end of the paper

Accepted XXX. Received YYY; in original form ZZZ

ABSTRACT

Rapid localisation and follow-up of gamma-ray bursts (GRBs) increasingly rely on low-latency triggers from new missions coupled to wide-field robotic optical facilities. We present the discovery and multi-wavelength follow-up of GRB 250818B, detected by the *Space Variable Objects Monitor* (SVOM) and localised optically by the Gravitational-wave Optical Transient Observer (GOTO). We compile and homogenise X-ray, optical/NIR, and radio data to build broadband light curves and spectral energy distributions. The afterglow is unusually luminous for a nominal short GRB, lying on the bright end of the short-GRB population in X-rays and optical and among the most luminous high-redshift short-GRB afterglows in the radio. MeerKAT detects the source at 3.1 GHz, while the Atacama Large Millimeter/submillimeter Array (ALMA) provides deep higher-frequency limits. Keck/LRIS spectroscopy shows continuum and metal absorption (Fe II, Mg II, Mg I), giving $z = 1.216$. Synchrotron forward-shock modelling favours a constant-density medium and strongly prefers refreshed (energy-injection) emission, well described by a two-component jet with $E_{K,\text{iso}} \sim 4 \times 10^{52}$ erg, $n_0 \sim 3.6 \text{ cm}^{-3}$, $\theta_j \simeq 0.10 \text{ rad}$ ($\sim 5.7^\circ$), and $p \simeq 1.64$. The host association is ambiguous: the nearest LS DR10 galaxy candidate ($r_{\text{AB}} \sim 24.7$) is offset by $\sim 4''$ ($\sim 34 \text{ kpc}$) with chance-alignment probability $P_{\text{cc}} \sim 0.2$, and current imaging does not exclude a fainter, near-coincident host. SED fitting of the candidate host suggests a low-mass galaxy. GRB 250818B highlights the power of rapid wide-field counterpart identification in the SVOM era, while host-association uncertainty can still limit offset-based interpretation.

Key words: (transients:) gamma-ray bursts – gamma-ray burst: individual: GRB 250818B

1 INTRODUCTION

Gamma-ray bursts (GRBs) were discovered serendipitously in the late 1960s as brief flashes of high-energy photons on the sky (Klebesadel et al. 1973). Subsequent observations have established GRBs as among the most luminous electromagnetic explosions in the Universe, with isotropic-equivalent γ -ray energy releases spanning $\sim 10^{51}$ – 10^{55} erg and durations from milliseconds to minutes (e.g. Piran 2004; Kumar & Zhang 2015; Wang et al. 2015a; Atteia et al. 2017; O'Connor et al. 2023; Cao et al. 2023; Pe'er 2024). A key step in organising this diversity was the recognition that the distribution of prompt-emission durations is bimodal, allowing GRBs

to be divided into two broad classes, “short” and “long”, typically separated at $T_{90} \simeq 2 \text{ s}$ ¹ (Kouveliotou et al. 1993). Long-duration GRBs are most commonly associated with the core collapse of massive, stripped-envelope stars, as demonstrated by numerous cases with accompanying broad-lined Type Ic supernovae (e.g. Galama et al. 1998; Hjorth et al. 2003; Woosley & Bloom 2006; Cano et al. 2017; Kumar et al. 2024), whereas short-duration GRBs are predominantly associated with compact-object mergers involving neutron stars and/or black holes (e.g. Eichler et al. 1989; Narayan et al. 1992; Tanaka 2016), supported by the detection of kilonovae and, most dramatically, by the joint GW170817/GRB 170817A event (e.g. Ab-
)

* E-mail: sergey.belkin@monash.edu (SB)

¹ T_{90} is the time interval containing 90% of the prompt γ -ray fluence.

bott et al. 2017; Goldstein et al. 2017; Savchenko et al. 2017; Pian et al. 2017; Troja et al. 2017; Valenti et al. 2017; Wang et al. 2017; Tanvir et al. 2017). At the same time, recent discoveries have revealed events that blur this simple mapping between duration and progenitor: the short (rest-frame $T_{90} \sim 0.5$ s) GRB 200826A showed a collapsar-like supernova (Zhang et al. 2021; Rossi et al. 2022), while long-duration bursts such as GRB 211211A (Rastinejad et al. 2022; Troja et al. 2022; Yang et al. 2022; Gompertz et al. 2023) and GRB 230307A (Dai et al. 2024; Levan et al. 2024; Sun et al. 2025) exhibit kilonova signatures indicative of compact-binary mergers. A further notable example is GRB 191019A, which has been interpreted as a merger produced by dynamical capture (Levan et al. 2023; Stratta et al. 2025), perhaps within the accretion disc of an active galactic nucleus (Lazzati et al. 2023). Taken together, these ‘‘hybrid’’ cases demonstrate that T_{90} and spectral hardness alone are imperfect discriminants of progenitor type, and that broadband afterglow and host-galaxy information are essential for interpreting the diversity of the GRB population and placing individual events in their physical context.

Broadband afterglow emission is commonly modelled as synchrotron radiation from a relativistic outflow decelerating in the circumburst medium, and encodes the kinetic energy, ambient density profile, microphysical parameters, and outflow geometry (e.g. Sari et al. 1998; Granot & Sari 2002; Panaiteescu & Kumar 2002; Miceli & Nava 2022). Multi-band light-curve and SED evolution can therefore test the simplest forward-shock scenario and reveal additional ingredients such as jet breaks and angular structure (e.g. Rhoads 1999; Sari & Piran 1999), refreshed shocks/energy injection (e.g. Rees & Mészáros 1998; Zhang & Mészáros 2002; Nousek et al. 2006), and reverse-shock or other extra components (e.g. Kobayashi 2000; Zhang et al. 2003). Host-galaxy context provides complementary constraints on the environment and potential progenitor channel through offsets and association statistics (e.g. Bloom et al. 2002; Fong & Berger 2013; Berger 2014; Blanchard et al. 2016; Heintz et al. 2020; Fong et al. 2022a; Nugent et al. 2024; Castrejon et al. 2025), but faint hosts near survey limits can complicate interpretation, particularly at $z \gtrsim 1$ where even moderate-luminosity galaxies begin to approach detectability limits in wide-field imaging. These considerations are especially relevant for events whose prompt-emission classification is uncertain or whose prompt constraints are incomplete, such that the afterglow and host environment carry a disproportionate share of the interpretive weight (e.g. Zhang et al. 2009; Bromberg et al. 2012, 2013).

The detection and characterisation of GRBs have been transformed by the advent of dedicated space-based observatories. The *Swift* mission detects ~ 90 GRBs per year (Lien et al. 2016) with the Burst Alert Telescope (BAT; Barthelmy et al. 2005) and provides rapid follow-up and arcsecond localisations of GRB afterglows with its narrow-field instruments, enabling systematic X-ray and UV/optical afterglow studies (Barthelmy et al. 2005; Burrows et al. 2005; Roming et al. 2005). Complementing this, the *Fermi* Gamma-ray Burst Monitor (GBM; Meegan et al. 2009; von Kienlin et al. 2020) discovers ~ 250 GRBs per year but typically with degree-scale localisation uncertainties (e.g. Connaughton et al. 2015; López et al. 2024), so bursts detected solely by GBM often rely on external facilities for afterglow identification and characterisation (e.g. Mong et al. 2021; Ahumada et al. 2022; Kumar et al. 2025a). More recently, new missions such as the *Einstein Probe* (EP; Yuan et al. 2015) and the *Space Variable Objects Monitor* (SVOM; Wei et al. 2016; Atteia et al. 2022), both launched in 2024, provide complementary coverage and low-latency triggering: *Einstein Probe* combines the Wide-field X-ray Telescope (WXT; 0.5–4 keV) with the Follow-up

X-ray Telescope (FXT; 0.5–10 keV), while *SVOM* detects GRBs with ECLAIRs (4–150 keV) and GRM (15 keV–5 MeV) and refines afterglows with *Swift*/XRT-like follow-up via MXT (0.2–10 keV) and the visible telescope VT (450–950 nm).

For GRBs discovered by wide-field γ -ray monitors, initial localisations can range from arcminutes (e.g. *SVOM*/ECLAIRs; typically $\lesssim 10'$, down to $\sim 3'$ for bright events) to tens of degrees (e.g. *Fermi*/GBM; localisation uncertainties can be ~ 10 –15°; (Connaughton et al. 2015)). Note that improved localisations can be obtained with more advanced methods (e.g. Burgess et al. 2018; Berlato et al. 2019). In the degree-scale regime in particular, efficiently identifying the optical afterglow requires ground-based facilities capable of tiling tens to hundreds of square degrees on timescales of minutes to a few hours. Wide-field, robotic optical surveys can fill this gap by rapidly covering the localisation region and performing real-time transient discovery.

The Gravitational-wave Optical Transient Observer (GOTO; Steeghs et al. 2022; Dyer et al. 2024) has been designed as an array of wide-field optical telescopes with sites at Roque de los Muchachos Observatory on La Palma and at Siding Spring Observatory in Australia, together providing near-continuous coverage of both hemispheres and an instantaneous field of view (FoV) of $\gtrsim 80$ deg 2 per site (two mounts). GOTO’s fast-response scheduling and wide FoV allow it to begin tiling degree-scale *Fermi*/GBM localisations and arcminute-scale *SVOM*/ECLAIRs error regions within minutes of a trigger, offering a complementary discovery channel to narrow-field facilities and helping to mitigate localisation-driven selection effects (e.g. Singer et al. 2015; Turpin et al. 2016). Previous campaigns have already demonstrated that GOTO can effectively search large *Fermi*/GBM error regions and identify GRB afterglows (e.g. Mong et al. 2021; Belkin et al. 2024; Kumar et al. 2025a), illustrating its potential as a discovery engine for GRBs with large high-energy localisations and motivating its use in conjunction with *SVOM* triggers such as GRB 250818B.

GRB 250818B provides a timely case study in the *SVOM* era: rapid triggering enabled extensive multi-wavelength follow-up. Throughout this work, we adopt the nominal short-GRB classification reported in discovery notices (Wang et al. 2025); our physical interpretation is driven primarily by the broadband afterglow behaviour and the host-galaxy context. Keck/LRIS afterglow spectroscopy established an absorption redshift of $z = 1.216$ (Fong et al. 2025), enabling rest-frame modelling of the afterglow and host properties.

At the same time, the host association is non-trivial: the nearest catalogued LS DR10 galaxy candidate is faint and offset by several arcseconds, while the imaging depth does not exclude a fainter, near-coincident host below the survey threshold. Because these scenarios imply very different physical offsets (and therefore limit the use of offset-based arguments), we place particular emphasis on constraints that arise directly from the broadband afterglow data. Specifically, we use the multi-band evolution to infer the circumburst environment and outflow dynamics, and to test whether a standard single-component forward-shock model is adequate or whether additional ingredients (e.g. energy injection and/or multiple components) are required. Where relevant, we comment on which inferences are insensitive to the uncertain physical offset and which depend on assumptions about the host association.

In this paper, we present the multi-wavelength follow-up of GRB 250818B and the identification of its optical afterglow by GOTO, and we use the resulting dataset to model the broadband afterglow and assess the host-galaxy association. In Section 2 we describe the available observations across X-ray, optical/NIR, and radio bands, together with the afterglow spectroscopy used to establish the

absorption redshift. In Section 3 we construct broadband light curves and SEDs, perform afterglow modelling with `afterglowpy` (via `redback`, including tests for energy injection and/or additional components), and analyse the putative host galaxy through association metrics (Bayesian and chance-coincidence statistics) and host-galaxy SED fitting with `Prospector`; we also construct a single-epoch optical afterglow SED to constrain line-of-sight extinction. In Section 4 we discuss the implications for the burst energetics, environment, and progenitor interpretation, including the host-association ambiguity and its impact on offset-based arguments. Our conclusions are summarised in Section 5.

Throughout this paper, we assume a flat Λ CDM cosmology with $H_0 = 70 \text{ km s}^{-1} \text{ Mpc}^{-1}$, $\Omega_m = 0.3$ and $\Omega_\Lambda = 0.7$, and quote magnitudes in the AB system unless stated otherwise.

2 OBSERVATIONS

At 2025-08-18T03:29:09 UTC (hereafter T_0), *SVOM*/ECLAIRs triggered on GRB 250818B and distributed via the General Coordinates Network (GCN) an on-board localisation with a 90% confidence radius of $7.44''$ (Wang et al. 2025). The burst also triggered *SVOM*/GRM at T_0 using a 1 s integration timescale (Wang et al. 2025).

We inspected the publicly available *Fermi*/GBM time-tagged event (TTE) data around T_0 and found that the spacecraft appears to have been traversing the South Atlantic Anomaly at that time; accordingly, no on-board or ground trigger was reported. A targeted search of the available TTE data also showed no significant excess.² We therefore do not report prompt-emission parameters from *Fermi*/GBM for this event, and no useful high-energy constraints from *Fermi*/LAT are available from public burst products.³

Wide-field optical imaging reported a fading counterpart within the *SVOM* localisation region, providing a precise position and enabling rapid coordination of follow-up (Sec. 2.2; Kumar et al. (2025c)). Subsequent *Swift*/XRT observations detected an uncatalogued X-ray source consistent with the *SVOM* localisation and coincident with the optical counterpart position (Ferro et al. 2025). The *SVOM* Visible Telescope (VT) also reported the same optical transient at a consistent position, and the *Einstein Probe* Follow-up X-ray Telescope (FXT) detected an X-ray source consistent with the counterpart (Li et al. 2025). These detections established the broadband afterglow and triggered an extensive multi-wavelength campaign from optical to radio. In the following subsections, we describe the high-energy, X-ray, optical/near-infrared, and radio datasets in more detail and outline the processing steps used to construct the broadband light curves and spectra employed in our analysis.

2.1 X-rays

The *Swift* X-Ray Telescope (XRT, 0.3–10 keV; Burrows et al. 2005) began follow-up observations of GRB 250818B at $T_0 + 1.7$ ks after the *SVOM* trigger. We use the XRT data to perform a time-resolved spectral analysis of the afterglow. Using the UK Swift Science Data Centre `SWIFTTOOLS` API (Evans et al. 2009)⁴, we downloaded and binned the data into bins with a signal-to-noise threshold of $S/N = 10$, which we adopt for spectral extraction and fitting in Section 3.2.

² GBM burst data products are publicly available via HEASARC: <https://heasarc.gsfc.nasa.gov/FTP/fermi/data/gbm/bursts/>.

³ LAT burst data products are publicly available via Fermi/SSC: <https://fermi.gsfc.nasa.gov/cgi-bin/ssc/LAT/LATDataQuery.cgi>.

⁴ <https://www.swift.ac.uk/API/>

2.2 Optical and NIR

GOTO responded to the *SVOM* alert and began observations of the *SVOM*/ECLAIRs localisation at $T_0 + 0.54$ h, obtaining a sequence of 4×90 s exposures in the wide L band (400–700 nm) between $T_0 + 0.54$ and $T_0 + 1.67$ h. Images were processed with the standard GOTO pipeline, including difference imaging against deeper templates and automated candidate filtering, followed by human vetting. These observations revealed a fading optical source, GOTO25fzq/AT 2025ukm (Kumar et al. 2025b), within the ECLAIRs 90% localisation region at R.A. = $03^{\text{h}}04^{\text{m}}13^{\text{s}}.52$, Dec. = $-03^{\circ}07'30.82''$ (J2000), with $L = 18.71 \pm 0.14$ mag at $T_0 + 0.54$ h and $L = 19.49 \pm 0.18$ mag (AB) at $T_0 + 1.67$ h. No source was detected at this position in pre-trigger GOTO images obtained 9.23 h before the burst, down to a 3σ limit of $L > 20.3$ mag, supporting the association with GRB 250818B (Kumar et al. 2025c).

The optical counterpart was subsequently detected by *SVOM*/VT in the VT_B band at $T_0 + 198.5$ and $T_0 + 3963.5$ s (Yao et al. 2025), by *Swift*/UVOT in the u band (Siegel & Swift/UVOT Team 2025), and by numerous ground-based facilities including KAIT (Zheng et al. 2025), NOT (Broe Bendtsen et al. 2025), SAO RAS (Moskvitin et al. 2025), TRT (An et al. 2025), Lesedi (Kumar et al. 2025d), LT (Dimple et al. 2025b), the GRANDMA/Kilonova-Catcher network (Hellot et al. 2025), and the Wendelstein FTW telescope (Busmann et al. 2025), providing multi-epoch photometry from minutes to several days after the burst.

The full optical/NIR dataset compiled in this work is given in Table A1. Where necessary, we converted literature photometry to the AB system using the offsets in Table A2 and corrected for Galactic extinction using the coefficients in Table A3. We also list the catalogue photometry of the candidate host galaxy in Table A4.

2.3 Radio and millimeter/submillimeter

We observed GRB 250818B with the MeerKAT radio telescope (in the Karoo desert, South Africa) through Director's Discretionary Time (DDT-20250822-GS-01 PI Schroeder) at mean frequencies of 1.3 GHz (0.856 GHz bandwidth) and 3.1 GHz (0.875 GHz bandwidth) for four epochs in each band, spanning mid-times of 5.0–32.1 days. J0323+0534 was used as a complex gain calibrator, and J0408-6545 was used as a flux calibrator for all observations and bands. We downloaded the SARAO Science Data Processor pipeline images for all observations and used the `pwkit/imtool` program (Williams et al. 2017) to measure the flux density and image RMS at the GOTO position. The radio afterglow of GRB 250818B is detected in the first 3.1 GHz observations, as reported in Schroeder et al. (2025d), and rises and fades over the course of the observations. The radio afterglow is only detected in the 1.3 GHz epoch at ~ 15 days.

We observed GRB 250818B with the Atacama Large Millimeter/Submillimeter Array (ALMA; Program 2024.1.01131.T, PI: W. Fong) in standard continuum mode with 4 GHz bandwidth at a mean frequency of 97.5 GHz for two epochs at mid-times of 10.14 days and 17.19 days, respectively. Both observations utilised J0312+0133 as a complex gain calibrator and J0327+0044 as a check source, while J0238+1636 and J0423-0120 were employed as the bandpass and flux density calibrators for the first and second epochs, respectively. We downloaded the final image products from the ALMA science archive. In the Quality Assurance Level 2 (QA2) images, no significant emission is seen in a $0.5''$ circle at the GOTO position. The image root-mean-square (rms) at the expected position of the target in the observations is $13.2 \mu\text{Jy}$ and $10.7 \mu\text{Jy}$, respectively.

The 36.8 GHz observations were carried out with the 22-m RT-22 radio telescope located in Simeiz (Crimea). The antenna has a half-power beam width of $\sim 100''$. Observations were performed in a beam-switching mode: the telescope was alternately pointed at the source with each of the two beam lobes produced by diagram modulation and having mutually orthogonal polarisations.

The antenna temperature of the source was determined from the difference between the radiometer outputs, each averaged over 30 s at the two antenna positions. For each epoch, we obtained a series of 200–250 such measurements, from which we computed the mean signal and its rms error. The measured antenna temperatures, corrected for atmospheric attenuation, were converted to flux densities by comparison with observations of standard calibration sources (Volvach et al. 2025). The resulting 36.8 GHz flux densities are listed in Table A5 and plotted in Fig. 2.

In addition, we include the 10 GHz flux density reported in GCN 41455 (Ricci et al. 2025b). As no uncertainty was provided, the point is shown as indicative in Fig. 2; for modelling, we assign an assumed uncertainty to prevent the fit from being dominated by this measurement.

2.4 Spectroscopy

We obtained optical spectroscopy of the GRB 250818B afterglow with the Low-Resolution Imaging Spectrograph (LRIS; Oke et al. 1995) mounted on the Keck I telescope (PI: C. Liu; Program O397). The observations comprised three 300 s exposures using the 400/3400 grism on the blue arm and the 400/8500 grating on the red arm, starting at 2025 August 18 14:10 UT (≈ 10.7 hr post-burst), under clear conditions with $\sim 0.9''$ seeing at airmass ~ 1.2 . The combined spectrum covers $\approx 3500 - 9500 \text{ \AA}$ in the observer frame (Fig. 1).

We reduce and co-add the data using the Python Spectroscopic Data Reduction Pipeline (PypeIt⁵; Prochaska et al. 2020b,a). PypeIt performs bias-subtraction, flat-fielding, cosmic ray masking, and wavelength calibrations on the individual frames. We perform 1D extraction and then co-add the spectrum. We then perform flux calibration and telluric correction, and corrected for foreground Milky Way extinction along the line of sight to the GRB, adopting $E(B - V)_{\text{MW}} = 0.0633$ mag from the Schlafly & Finkbeiner recalibration of the Schlegel et al. dust map (Schlegel et al. 1998; Schlafly & Finkbeiner 2011), and an $R_V = 3.1$ Milky Way extinction law (Fitzpatrick & Massa 2007). The continuum is detected across most of the wavelength range and exhibits several prominent metal absorption features.

We determine the redshift by identifying a consistent set of metal absorption lines, including Fe II $\lambda\lambda 2344, 2374, 2382$, the Mg II doublet $\lambda\lambda 2796, 2803$, and Mg I $\lambda 2852$. We refine the redshift by maximising the alignment of these transitions with absorption troughs in the spectrum, yielding $z = 1.216$. We adopt this value as the redshift of GRB 250818B throughout the paper.

3 ANALYSIS AND RESULTS

3.1 Broadband Light-Curve Construction

For our analysis, we compiled all publicly available photometric measurements reported in these GCN circulars and in our own follow-up

before constructing the optical/near-infrared light curves. All optical and near-infrared measurements were homogenised onto the AB magnitude system (Oke & Gunn 1983). For data reported in the Vega system, we applied fixed offsets of the form $m_{\text{AB}} = m_{\text{Vega}} + \Delta m$ appropriate for each filter. For Johnson–Cousins *UBVRI* and near-infrared *JHK_s* filters, as well as Sloan-like *griz*, we adopted the standard Vega-to-AB offsets from Blanton & Roweis (2007). For the *Swift*/UVOT *u*, *b* and *v* bands we used the AB–Vega corrections from the UVOT photometric calibration (e.g. Poole et al. 2008; Breeveld et al. 2011). The values of Δm used in this work are listed in Table A2. Measurements already reported in AB magnitudes were left unchanged.

We corrected all photometry for Milky Way extinction using a single colour excess $E(B - V)_{\text{MW}} = 0.0633$ mag along the GRB sightline (consistent with Section 2.4), adopting the Schlafly & Finkbeiner recalibration of the Schlegel et al. dust map (Schlegel et al. 1998; Schlafly & Finkbeiner 2011). We assumed a standard $R_V = 3.1$ Milky Way extinction curve. For Sloan-like *ugriz* filters we used the tabulated coefficients $A_{\lambda}/E(B - V)$ from Schlafly & Finkbeiner (2011); for Johnson–Cousins *UBVRI* and near-infrared bands we used coefficients appropriate for an $R_V = 3.1$ Milky Way law (e.g. Fitzpatrick 1999). For the *Swift*/UVOT filters we employed the passband-integrated $A_{\lambda}/E(B - V)$ values from Yi et al. (2023), rescaled to be consistent with our adopted $E(B - V)$. For non-standard filters, we adopted approximate coefficients: for the GOTO *L* band, we used $A_L \approx 0.997 A_V$, and for the *SVOM/VT_B* band we set A_{VT_B} to the average of the SDSS *g* and *r* coefficients. The resulting A_{λ} values for the filters used in this work are given in Table A3.

After correcting for Galactic extinction, we converted all magnitudes to monochromatic flux densities F_{ν} following the definition of the AB system (Oke & Gunn 1983), adopting a zeropoint $F_{\nu,0} = 3631$ Jy. For non-detections, we converted the limiting magnitudes to 3σ upper limits on F_{ν} . The resulting extinction-corrected optical/near-infrared flux densities, together with the *Swift*/XRT and radio measurements (Sec. 2.1, 2.3), are shown in Fig. 2 and form the basis for the afterglow analysis in the following subsections.

3.2 X-ray Spectral Analysis

There were a total of three intervals found from the $\text{SNR} = 10$ binning, from which spectra were extracted and fit simultaneously. We fit the *Swift*/XRT spectra to a power-law model using PyXSPEC version 2.1.4 (xsSPEC version 12.15.0) using Cash statistic (Cash 1979) and a Wilms solar abundance (Wilms et al. 2000). The absorption from the neutral hydrogen column along the line of sight is accounted for using a model components of the form $\text{TBABS}^* \text{ZTBABS}^* \text{CFLUX}^* \text{POWERLAW}$. TBABS accounts for the neutral hydrogen in the Milky Way, fixed to $N_{\text{H, Gal}} = 6.49 \times 10^{20} \text{ cm}^{-2}$ (Willingale et al. 2013), ZTBABS parameterises the absorption contribution from the host ($N_{\text{H, Intr}}$) with redshift fixed to the spectroscopic value of 1.216, and CFLUX calculates the flux of the model components. Two sets of fitting were performed: one calculating the unabsorbed flux (with the model format as above), and another calculating the absorbed flux ($\text{CFLUX}^* \text{TBABS}^* \text{ZTBABS}^* \text{POWERLAW}$). $N_{\text{H, Intr}}$ was tied between each spectrum as it is not expected to evolve with time, while the photon index Γ was left free to vary between spectra, as was the flux (calculated between 0.3 – 10 keV). The absorbed power-law model provides an adequate description of the data ($\text{CSTAT/DoF} = 0.24$), with no systematic residuals; given the limited photon statistics, we therefore do not explore more complex spectral models. The time intervals for the extracted spectra and the evolution of Γ are shown in Fig. 3. We further investigated spectral variability using finer spec-

⁵ <https://pypeit.readthedocs.io/en/latest/>

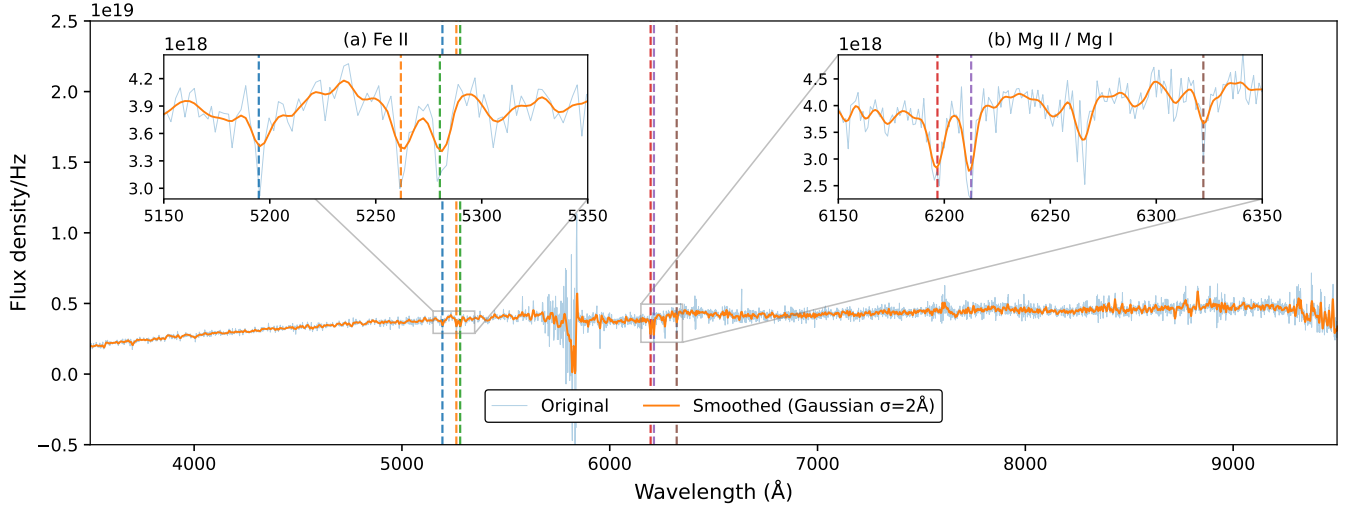


Figure 1. Keck I/LRIS flux-calibrated, Galactic-extinction-corrected spectrum of the optical afterglow of GRB 250818B obtained at ≈ 10.7 hr post-burst; wavelengths are shown in the observer frame. The light-blue curve shows the original spectrum and the orange curve shows a Gaussian-smoothed version ($\sigma = 2 \text{ \AA}$) for display purposes. Vertical dashed lines mark the expected observed-frame wavelengths of the Fe II $\lambda\lambda 2344, 2374, 2382$, Mg II $\lambda\lambda 2796, 2803$, and Mg I $\lambda 2852$ absorption transitions at the best-fit redshift $z = 1.216$. Insets highlight the Fe II and Mg II/Mg I regions used to refine the redshift estimate.

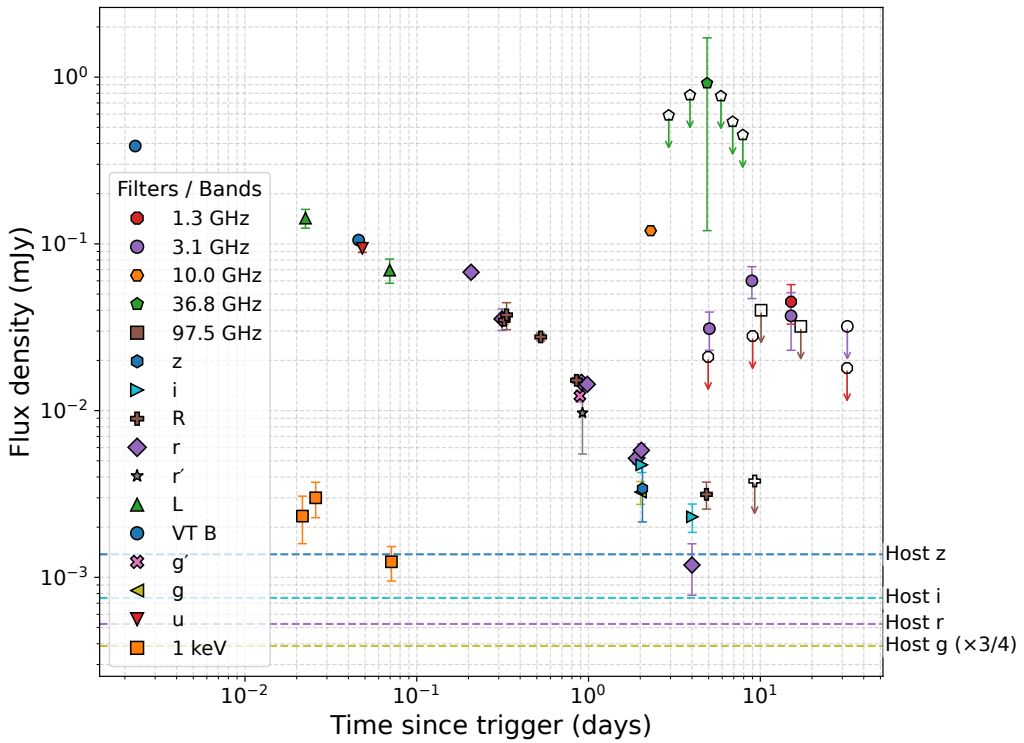


Figure 2. Multi-wavelength light curve of GRB 250818B, showing X-ray, optical/near-infrared, and radio flux densities as a function of time since the *SVOM*/ECLAIRs trigger. Optical points are corrected for Galactic extinction and converted to AB flux densities. Triangles with arrows indicate 3σ upper limits. The host-galaxy fluxes shown in g , r , i , and z correspond to the LS DR10 candidate host galaxy (Tractor objid 5790) discussed in Section 3.4.1. For visual clarity, the plotted g -band host level is vertically offset by a factor of 3/4 to avoid overlap with the r -band host level; all analysis uses the unscaled host flux.

tral bins with $\text{SNR} = 5$, but found no evidence for additional spectral evolution due to the larger measurement uncertainties resulting from the lower-significance bins.

3.3 Afterglow

3.3.1 X-ray afterglow brightness in context

To place the early-time X-ray behaviour of GRB 250818B in context, we compared its *Swift*/XRT 0.3–10 keV afterglow to the population of *Swift*-detected events using UKSSDC XRT light curves (Fig. 4).

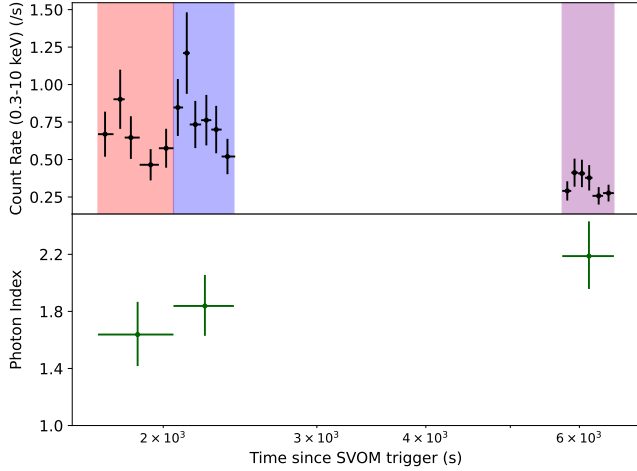


Figure 3. Top: XRT count rate light curve of the three flaring episodes, where the highlighted sections indicate the three $\text{SNR} = 10$ spectral bins. The late-time XRT data at ~ 3.35 d does not meet the SNR threshold and so is not included in the spectral analysis. Bottom: evolution of the best-fit photon index with time.

Short-duration and long-duration bursts are shown in darker and lighter grey, respectively, using a T_{90} -based duration classification from the *Swift*/BAT GRB summary catalogue. Bursts whose BAT $T_{90} \pm \sigma$ interval straddles 2 s are flagged as “borderline” between the two classes and plotted in an intermediate grey shade; they are not included when computing the short-GRB medians quoted below. In this view, GRB 250818B sits on the bright end of the short-GRB distribution at early times. At the three epochs corresponding to our $\text{SNR}=10$ XRT spectral bins (1869, 2232, and 6153 s; Table A6), its unabsorbed flux is ~ 12.7 , ~ 17.1 , and ~ 9.5 times higher than the median 0.3–10 keV flux of the *Swift* short-duration sample with coverage at these times ($N_{\text{short}} = 46, 47$, and 35, respectively). While this comparison is made in the observer frame and does not account for redshift or sample heterogeneity, it supports the qualitative impression that the early afterglow of GRB 250818B is unusually X-ray bright relative to typical *Swift* short-duration GRBs.

The elevated early-time X-ray flux of GRB 250818B could reflect a combination of higher-than-average afterglow energetics, and/or a favourable viewing geometry (e.g., a more on-axis sightline or a narrow/structured jet component; e.g. [Sari et al. 1998](#); [Granot & Sari 2002](#); [Panaitescu & Kumar 2002](#)). In the standard forward-shock synchrotron framework, if the X-ray band lies above the cooling break ($\nu_X > \nu_c$; as suggested by the optical–X-ray spectral slopes), the X-ray flux depends only weakly on the external density, while density variations primarily affect the location and evolution of ν_c and hence the optical/radio behaviour (e.g. [Sari et al. 1998](#); [Granot & Sari 2002](#)). If instead ν_c lies above the X-ray band ($\nu_c > \nu_X$), the X-ray flux would have a stronger dependence on the circumburst environment and the expected spectral/temporal indices would differ, but this appears less consistent with the observed broadband slopes. A contribution from early-time energy injection is also plausible (e.g. [Rees & Mészáros 1998](#); [Zhang & Mészáros 2002](#); [Nousek et al. 2006](#)); however, the X-ray comparison is not diagnostic, and distinguishing between these possibilities requires dedicated broadband modelling (and, where possible, rest-frame comparisons).

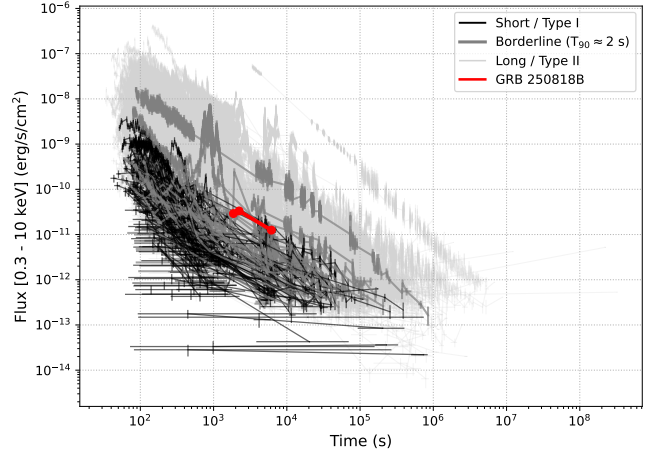


Figure 4. *Swift*/XRT observer-frame 0.3–10 keV afterglow comparison for GRB 250818B. Grey curves show 0.3–10 keV XRT light curves of *Swift*-detected GRBs downloaded from the UKSSDC repository. Short-duration bursts are highlighted in darker grey, while long-duration events are shown in light grey, using a *Swift*/BAT T_{90} -based duration classification from the *Swift*/BAT GRB summary catalogue (excluding events with unidentified T_{90}). Bursts whose BAT $T_{90} \pm \sigma$ interval straddles 2 s (“borderline” between short and long) are plotted in medium grey. Red points show the unabsorbed 0.3–10 keV fluxes of GRB 250818B from our XRT spectral analysis with $\text{SNR}=10$ binning (Table A6); the red line connects the measurements to guide the eye. Times are measured relative to the prompt trigger in the observer frame (BAT trigger for the *Swift* comparison sample; SVOM/ECLAIRs T_0 for GRB 250818B).

3.3.2 Optical afterglow brightness in context

To place the optical afterglow of GRB 250818B in the broader GRB population, we compare its observer-frame *R*-band evolution with the literature compilation of [Kann et al. \(2006, 2010, 2011\)](#) and the sGRB sample of [Nicuesa Guelbenzu et al. \(2012\)](#). For the [Kann et al. \(2011\)](#) comparison sample, we adopt the Type I/Type II classifications reported therein (a progenitor-motivated scheme that is not strictly equivalent to a T_{90} -based short/long division). Given the limited number of direct *R*-band measurements for GRB 250818B, we show the *R*-band projection of our simultaneous multiband SBPL fit (Fig. 5). All magnitudes are corrected for Galactic extinction.

At the epochs corresponding to our *R*-band observations (0.32, 0.33, 0.53 and 0.85 d), we interpolate the comparison light curves in $\log t$ -magnitude space, using only events with data bracketing each epoch (yielding $N_{\text{all}} \approx 136 - 142$ and $N_{\text{short}} \approx 29 - 31$). The full sample spans $R \approx 14.2 - 26.7$ mag with medians of $R \approx 20.4 - 21.3$ mag, while the short/Type I subset has fainter medians of $R \approx 22.6 - 23.9$ mag. GRB 250818B has $R \approx 19.9 - 20.9$ mag at these times, placing it only $\sim 0.3 - 0.6$ mag brighter than the median of the overall population, but $\sim 2.7 - 3.0$ mag brighter than the median of the short/Type I subset. For reference, relative to the long/Type II subset alone, GRB 250818B is within $\lesssim 0.2$ mag of the median at these epochs. Thus, although GRB 250818B is identified as a short GRB, its optical afterglow lies on the bright end of the sGRB distribution at $\sim 0.3 - 0.9$ d, while remaining broadly consistent with the full comparison sample (dominated by long GRBs) in the same band.

Having a securely defined redshift ($z = 1.216$) for GRB 250818B, we can also express its optical afterglow brightness in the luminosity-space framework commonly used for short-GRB comparisons. Using our Galactic-extinction-corrected observer-frame *R*-band SBPL

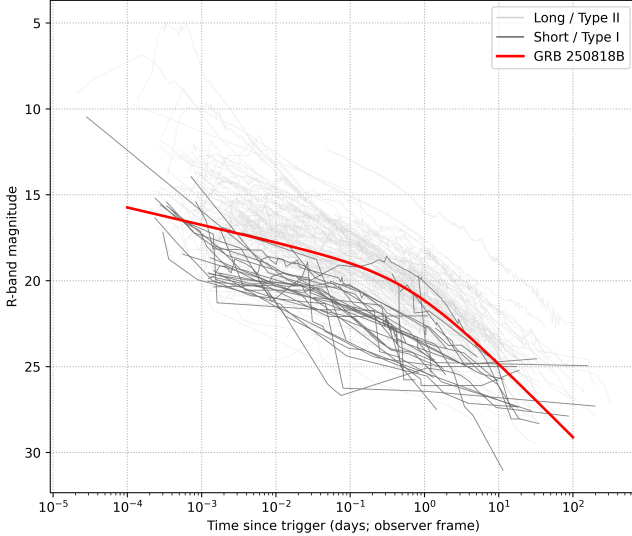


Figure 5. Observer-frame R -band afterglow comparison for GRB 250818B. Grey curves show literature R -band afterglow light curves compiled from Kann et al. (2006, 2010, 2011); Nicuera Guelbenzu et al. (2012). The short/Type I subset (as classified in Kann et al. 2011) is highlighted in darker grey, while long/Type II events are shown in light grey. The red curve shows the R -band model of GRB 250818B derived from our simultaneous multi-band SBPL fit. All magnitudes are corrected for Galactic extinction.

model and converting to νL_ν at the corresponding rest-frame frequency, we find $\log_{10}(\nu L_\nu) \approx 45.26$ at a rest-frame time $\delta t_{\text{RF}} = 3$ hr (i.e. the observer-frame time divided by $1+z$; $\nu L_\nu \approx 1.8 \times 10^{45} \text{ erg s}^{-1}$), declining to $\log_{10}(\nu L_\nu) \approx 44.24$ at $\delta t_{\text{RF}} = 1$ day. These values place GRB 250818B toward the bright end of the short-GRB optical afterglow distribution at a common rest-frame epoch (Castrejon et al. 2025), consistent with its location on the bright tail in the observer-frame R -band comparison shown in Fig. 5.

3.3.3 Optical SED and line-of-sight extinction

To constrain the line-of-sight extinction in the host galaxy, we constructed a single-epoch optical SED at $t_{\text{ref}} = 2.035$ d after the trigger using nearly contemporaneous LT gri photometry and late-time DECam imaging to subtract the host contribution (Sec. 3.4.3). Throughout this subsection, we adopt the standard convention $F_\nu \propto \nu^{-\beta}$ for the flux-density spectral index β . For reference, the X-ray photon index Γ (defined by the photon spectrum $N_E \equiv dN/dE \propto E^{-\Gamma}$) corresponds to $\beta_X = \Gamma - 1$.

All measurements were corrected for Galactic foreground extinction (Schlafly & Finkbeiner 2011). We subtracted the DECam host flux in each band from the corresponding LT flux, propagated the statistical errors in quadrature, and added a 5% fractional uncertainty in flux to account for cross-calibration and host-subtraction systematics. The resulting host-subtracted flux densities are shown in Fig. 6 as a function of observed frequency (bottom axis; the top axis gives the corresponding rest-frame wavelength at $z = 1.216$). The z -band point is plotted for reference but excluded from the fit because its uncertainty is dominated by low S/N and host-subtraction systematics.

We model the SED as a power law modified by dust extinction in the host galaxy,

$$F_\nu(\nu_{\text{obs}}) = C \left(\frac{\nu_{\text{obs}}}{\nu_0} \right)^{-\beta} 10^{-0.4 A_V k(\lambda_{\text{rest}})}, \quad (1)$$

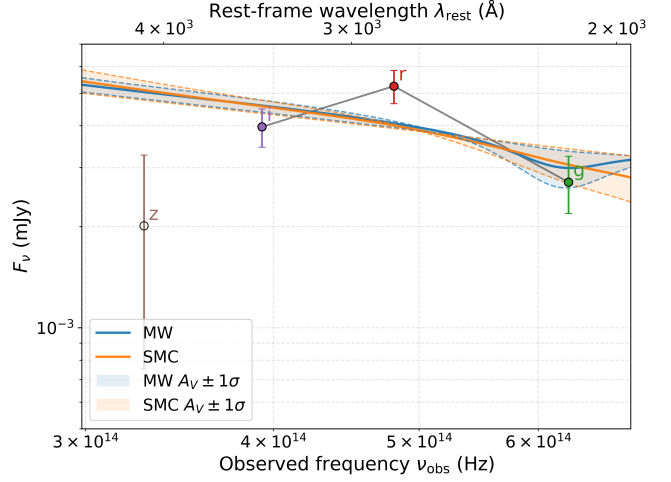


Figure 6. Host-subtracted optical SED of GRB 250818B at $t \approx 2.0$ d. Filled points show the host-subtracted gri flux densities; the open z point is shown for comparison but excluded from the fit. Solid curves show the best-fitting dust-attenuated power-law models for a Milky Way extinction law (F99; $R_V = 3.1$) and an SMC Bar law (G03; $R_V = 2.74$) at $z = 1.216$. Dashed curves and shaded bands illustrate the effect of varying the fitted A_V by $\pm 1\sigma$ (with the power-law normalisation and slope refit at fixed A_V). The two laws are nearly indistinguishable across the observed optical bands, and the host-frame extinction is weakly constrained ($A_V \sim 0.2$).

where C is a normalisation at reference frequency ν_0 , β is the intrinsic optical spectral index, A_V is the host-frame V -band extinction, and $k(\lambda_{\text{rest}}) \equiv A_\lambda/A_V$ is the extinction curve evaluated at $\lambda_{\text{rest}} = c/[\nu_{\text{obs}}(1+z)]$. We consider a Milky Way law (Fitzpatrick 1999, F99) with fixed $R_V = 3.1$ and an SMC Bar law (Gordon et al. 2003, G03) with $R_V = 2.74$, as implemented in `dust_extinction` (Gordon 2024). We do not consider the M14/LMC family further because it is undefined below $\lambda_{\text{rest}} \sim 3000$ Å, whereas at $z = 1.216$ the observed g and r bands probe $\lambda_{\text{rest}} \lesssim 3000$ Å.

To reduce the strong β - A_V degeneracy inherent to three-band photometry, we incorporate an X-ray-informed prior on β . Our time-resolved *Swift*/XRT spectroscopy yields photon indices $\Gamma_X \approx 1.6$ – 2.2 , with a weighted mean $\langle \Gamma_X \rangle \approx 1.9$, i.e. $\beta_X \approx 0.9$ (Sec. 2.1). In the slow-cooling synchrotron model the spectrum steepens by $\Delta\beta = 0.5$ across the cooling break, so a physically plausible configuration is $\nu_{\text{opt}} < \nu_c < \nu_X$, which would imply $\beta_{\text{opt}} \approx \beta_X - 0.5 \approx 0.4$. We therefore adopt a broad Gaussian prior $\beta \sim \mathcal{N}(0.40, 0.30)$, which also allows the possibility that optical and X-rays lie on the same spectral segment. We fit Eq. 1 in flux space using χ^2 minimisation (`scipy.optimize.least_squares`; Virtanen et al. 2020), with the prior implemented as an additional term in the residual vector. The XRT flux itself is not used in the optical extinction fit.

Fitting the host-subtracted gri SED yields consistent results for both extinction laws (Fig. 6). For the MW law we obtain $A_V^{\text{host}} = 0.22 \pm 0.18$ mag and $\beta_{\text{opt}} = 0.28 \pm 0.30$ ($\chi^2/\text{dof} \approx 5.67/1$); for the SMC law we find $A_V^{\text{host}} = 0.20 \pm 0.19$ mag and $\beta_{\text{opt}} = 0.31 \pm 0.30$ ($\chi^2/\text{dof} \approx 6.14/1$). Given that the fit is constrained by only three photometric points (one degree of freedom) and is sensitive to host-subtraction and cross-calibration systematics, these numerical values should be regarded as indicative rather than definitive. The relatively large χ^2 values and the sparse three-point SED emphasise that A_V^{host} is only weakly constrained and sensitive to systematics (Fig. 6). Nonetheless, both laws point to low-to-moderate extinction and remain compatible with $A_V^{\text{host}} \approx 0$ within $\sim 1\sigma$.

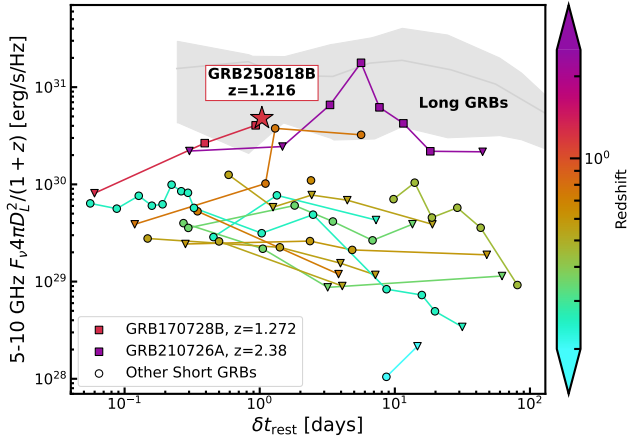


Figure 7. 5–10 GHz (observer frame) afterglow luminosity vs rest frame time of radio detected short GRBs (Berger et al. 2005; Soderberg et al. 2006; Panaitescu 2006; Fong et al. 2014, 2015; Lamb et al. 2019; Fong et al. 2021; Laskar et al. 2022; Schroeder et al. 2024, 2025a; Anderson et al. 2025; Angulo-Valdez et al. 2025; Gulati et al. 2025; Ricci et al. 2025a), with points colored by redshift (redshifts from Fong et al. 2022b; Schroeder et al. 2024; Nugent et al. 2024; Angulo-Valdez et al. 2025; Schroeder et al. 2025a). Triangles represent 3σ upper limits. The 10 GHz afterglow of GRB 250818B (Ricci et al. 2025b) is represented as a star, and the two other radio detected short GRBs at $z > 1$ (GRB 170728B at $z = 1.272$ and GRB 210726A at $z = 2.38$) are represented as squares. Also shown is the typical radio afterglow range for long GRBs (shaded grey, Chandra & Frail 2012).

We also investigated joint optical+X-ray SED fits at the same epoch imposing $\beta_X = \beta_{\text{opt}} + 0.5$, as expected for a standard slow-cooling synchrotron spectrum when the cooling break lies between the optical and X-ray bands (e.g. Sari et al. 1998; Granot & Sari 2002). However, at $t \approx 2$ d the contemporaneous 1 keV flux is only a marginal detection and does not meet the quality cuts adopted for our X-ray analysis. Including this point does not materially change the best-fitting A_V , but it introduces additional assumptions (e.g. the location of v_c , the validity of the fixed $\Delta\beta = 0.5$ relation, and potential X-ray absorption/cross-calibration systematics) that can dominate the inference when the X-ray constraint is weak. We therefore adopt the optical-only fit with the XRT-informed β prior as our baseline.

3.3.4 Radio afterglow brightness in context

GRB 250818B is only the third short GRB to have a detected radio afterglow at $z > 1$, with the other two short GRBs being GRB 170728B (with a spectroscopic redshift of $z = 1.272 \pm 0.002$; Fong et al. 2022b) and GRB 210726A (with a photometric redshift of $z = 2.38^{+0.39}_{-0.75}$; Schroeder et al. 2024). As a result, at a spectroscopic redshift of $z = 1.216$, the radio afterglow of GRB 250818B is among the most luminous in the short GRB population, with a 10 GHz luminosity of $\sim 5 \times 10^{30}$ erg s $^{-1}$ Hz $^{-1}$ at a rest-frame time of $\delta t_{\text{RF}} \approx 1$ days, based on the 10 GHz measurement reported in GCN 41455 (no formal uncertainty was provided) (Ricci et al. 2025b). In comparison, most radio detected short GRBs have 10 GHz afterglow luminosities of $\sim 2 - 8 \times 10^{29}$ erg s $^{-1}$ Hz $^{-1}$ at similar rest-frame times (Fig. 7). GRB 170728B and GRB 250221A (spectroscopic redshift of $z = 0.768$; Angulo-Valdez et al. 2025) have comparable radio afterglow luminosities to GRB 250818B at $\delta t \approx 1$ day, whereas GRB 210726A peaked at $\sim 2 \times 10^{31}$ erg s $^{-1}$ Hz $^{-1}$ at a rest frame time of $\delta t_{\text{RF}} \approx 6$ days (Fig. 7). Several of the most radio-luminous short GRBs have been modelled with additional components beyond

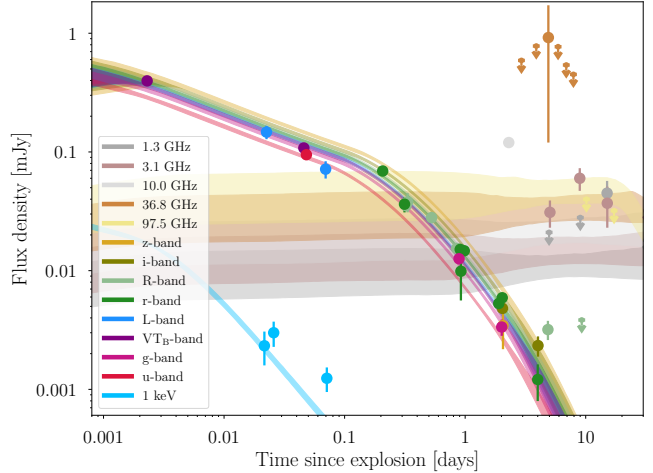


Figure 8. The 1σ confidence interval for light curves drawn from the posterior sample for a simple top-hat afterglow model from afterglowpy.

a single forward shock (e.g. energy injection and/or reverse-shock contributions; see Sec. 4 for further discussion). The MeerKAT detection of GRB 250818B adds to the growing population of short GRBs securely detected at $\lesssim 5$ GHz, now totaling 7 (GRBs 140903A, 210726A, 230217A, 231117A, 250520A, 250704B, and 250818B; Nayana & Chandra 2014; Schroeder et al. 2024; Chastain et al. 2024; Anderson et al. 2024; Schroeder et al. 2025a,b,c; Anderson et al. 2025). A tentative very-low-frequency radio counterpart has also been reported for GRB 201006A (Rowlinson et al. 2024). The late-time rise of the 1.3 GHz afterglow is reminiscent of GRB 210726A (Schroeder et al. 2024), and highlights the utility of low-frequency ($\lesssim 5$ GHz) observations extended to later times ($\gtrsim 10$ days) to capture the afterglow peak as the synchrotron spectrum evolves to lower frequencies (e.g. Sari et al. 1998; Granot & Sari 2002). In particular, when prompt-emission constraints are weak or unavailable, the afterglow becomes the primary handle on the explosion energetics and environment. Locating the low-frequency peak and its time evolution anchors the synchrotron spectrum (i.e. the characteristic frequency and flux scale), helping to constrain the kinetic energy and circumburst density and to reduce degeneracies among the microphysical parameters in broadband modelling.

Measuring the peak time and flux at these frequencies provides direct leverage on the afterglow energetics and circumburst environment (and helps break degeneracies in broadband modelling), which is particularly valuable when prompt-emission constraints are weak or unavailable.

3.3.5 afterglowpy Baseline Modelling

A rapid afterglow modelling tool is provided by afterglowpy (Ryan et al. 2020), and in combination with redback (Sarin et al. 2024) this enables end-to-end modelling and inference. Using the available detections and upper limits, we fit a simple uniform (top-hat) jet model to the data. We sample the posterior with the nested sampler nessai (Williams et al. 2023), adopting the priors listed in Table 1. The resulting 1σ credible intervals for each observing band are shown in Fig. 8.

Although these fits return parameters that are consistent with expectations for GRB afterglows, it should be noted that the posterior distribution for p is pushing up against the imposed lower boundary of $p = 2$. This suggests that, within this simple top-hat forward-shock

Table 1. The model parameter prior distributions and constraints for the `afterglowpy` and the `twocomponent_redback` model fit to data via `redback` using the `nessai` sampler. The model parameters are: θ_{obs} , the observer angle from the jet central axis; E_{iso} , the initial isotropic equivalent jet kinetic energy for a point at the jet axis; θ_c , the jet core half-opening angle; θ_j , the maximum angular extent of the jet; n_0 , the ambient particle number density; p , the accelerated electron distribution index within the afterglow shock; ε_e , the fraction of energy in shocked electrons; ε_B , the fraction of energy in the shock-induced magnetic field; ξ_N , the shocked electron, synchrotron participation fraction; Γ_0 , the initial bulk Lorentz factor of the jet core; γ_{col} , the Lorentz factor of the impulsive shell when energy injection (refreshed) commences; e_t , the fractional increase in the energy of the core due to energy injection; $\Gamma_{0,2C}$, the initial bulk Lorentz factor of the second, sheath component; e_s , the fraction of the core isotropic kinetic energy in the sheath.

| Parameter | Prior | Afterglowpy | | twocomponent_redback | | |
|-----------------------------|------------|------------------------------------------|-------------------------|----------------------|------------------------------------|---------------------------|
| | | Condition | Posterior | Prior | Condition | Posterior |
| θ_{obs} (rad) | $0, \pi/2$ | $\theta_{\text{obs}}/\theta_j \leq 3/2$ | $0.07^{+0.03}_{-0.02}$ | 0 | fixed | 0 |
| $\log E_{\text{iso}}$ (erg) | 44, 54 | - | $52.48^{+0.23}_{-0.22}$ | 44, 54 | - | $52.60^{+0.12}_{-0.13}$ |
| θ_c (rad) | - | - | - | $0, 0.1$ | $\theta_c < \theta_j$ | $0.07^{+0.01}_{-0.01}$ |
| θ_j (rad) | $0, 0.3$ | - | $0.07^{+0.03}_{-0.02}$ | $0.02, 0.12$ | $\theta_j > \theta_c$ | $0.10^{+0.01}_{-0.02}$ |
| $\log n_0$ (cm $^{-3}$) | -5, 2 | - | $-0.21^{+0.93}_{-0.67}$ | -5, 2 | - | $0.56^{+0.07}_{-0.07}$ |
| p | 2, 3 | - | $2.05^{+0.03}_{-0.02}$ | 1.4, 3.1 | - | $1.64^{+0.05}_{-0.05}$ |
| $\log \varepsilon_e$ | -5, 0 | $\varepsilon_e + \varepsilon_B \leq 0.9$ | $-0.26^{+0.13}_{-0.19}$ | -1 | fixed | -1 |
| $\log \varepsilon_B$ | -5, 0 | $\varepsilon_e - \varepsilon_B > 0.0$ | $-1.12^{+0.43}_{-0.62}$ | -2 | fixed | -2 |
| ξ_N | 0.1, 1 | - | $0.16^{+0.08}_{-0.04}$ | 1 | fixed | 1 |
| Γ_0 | 100, 2000 | - | 1055^{+634}_{-634} | 40, 150 | - | $130.9^{+9.6}_{-9.7}$ |
| γ_{col} | - | - | - | 2, 50 | $\gamma_{\text{col}} < \Gamma_0/2$ | $41.9^{+5.6}_{-7.7}$ |
| e_t | - | - | - | 1, 50 | - | $25.81^{+16.01}_{-16.07}$ |
| $\Gamma_{0,2C}$ | - | - | - | 3, 20 | - | $6.0^{+1.9}_{-1.2}$ |
| e_s | - | - | - | 0.1, 10 | - | $1.03^{+1.72}_{-0.74}$ |
| Information | | ln Bayes | | Information | | ln Bayes |
| 25.82 | | -42.537 | | 21.98 | | 42.537 |

model family, the data would prefer a harder electron spectrum (formally $p < 2$); we therefore interpret this as an indication of model tension rather than a precise physical constraint on p . The baseline `afterglowpy` top-hat model does not reproduce the full X-ray evolution, with noticeable mismatch after the first data point (see Fig. 8). The optical data from ~ 3 days are additionally in excess of the model light curve, suggesting either an additional component to the emission at late times or limitations of the simple top-hat forward-shock description. The radio data and limits sit well above the model radio posterior distribution, which does not violate the limits used; however, the model underpredicts by $> 1\sigma$ uncertainty the 36.8 GHz detection at $\sim 4 - 5$ days, noting that this detection has a large uncertainty.

3.3.6 `redback` energy-injection test and model comparison

The variability within the afterglow indicates that there may have been a period of energy injection. Additionally, the late data appears to indicate either a further period of injection or an energetic wider component coming into view (i.e., [Takahashi & Ioka 2021](#), a sheath surrounding a hollow/lower-energy jet). To demonstrate the viability of this model, we pick fiducial model parameters informed via the `afterglowpy` fit, however, setting $p = 1.8$ (i.e., $p < 2$), isotropic kinetic energy, $E_{\text{iso}} = 3.15 \times 10^{52}$ erg, an ambient particle number density, $n_0 = 1 \text{ cm}^{-3}$, and fixing microphysical parameters $\varepsilon_e = 0.1$, $\varepsilon_B = 0.01$, $\xi_N = 1$, and the bulk Lorentz factor, $\Gamma_0 = 140$, for the fiducial illustrative model shown as the dotted curve in Fig. 9. We adopt $\varepsilon_B = 0.01$ as a conventional fiducial choice often used when the microphysics are not directly constrained (e.g. [Fong et al. 2015](#)); however, published estimates of ε_B span several orders of magnitude (e.g. [Hennessy et al. 2025](#)). The normalisation of this illustrative curve (and the implied energy/density scalings) should therefore be regarded as conditional on the assumed microphysical parameters.

We use a refreshed shock, two-component model (see e.g., [Lamb](#)

& [Kobayashi 2017](#); [Lamb et al. 2018, 2020](#)) from `redback`, the `twocomponent_redback` from their model library, and set additional parameters as: the Lorentz factor of the impulsive shell at collision, $\gamma_{\text{col}} = 28$, the total factor by which energy increases, $e_t = 3.5$, assuming an instantaneous injection, and a second component with a bulk Lorentz factor, $\Gamma_{0,2C} = 12$, with a factor, $e_s = 2.5$, of the isotropic equivalent energy within the core region. In this two-component configuration, a relativistic core is surrounded by a slower, baryon-loaded sheath extending to θ_j ; for this fit, we assume an on-axis viewing geometry ($\theta_{\text{obs}} = 0$). For the fiducial proof-of-principle model (dotted curve in Fig. 9), we adopted narrow opening angles ($\theta_c \sim 2.2^\circ$, $\theta_j \sim 2.5^\circ$) to reproduce the apparent break in the light curve. For the posterior fit, the sampler prefers broader angles; we therefore quote the fitted values from Table 1 (median $\theta_c \approx 0.07$ rad and $\theta_j \approx 0.10$ rad). This model is shown against the data in Fig. 9; additionally plotted are the confidence intervals inferred via 250 random draws from the posterior distribution fit for this model – the prior was chosen based on our fiducial parameters and is listed, along with posterior ranges, in Table 1.

The sampler, `nessai`, provides a log Evidence and an information score (see, [Williams et al. 2021](#), for details); despite the increased number of parameters for the `twocomponent_redback` model, this is the preferred model. The respective information scores and the log Bayes factor for model preference between the two are shown – where the preferred model will have the lowest value and the most positive difference in log evidence, respectively (see Table 1).

3.4 Host Galaxy

3.4.1 Association

We searched the Legacy Survey (LS DR10; [Dey et al. 2019](#)) catalogue around the position of GRB 250818B and identified a faint galaxy at $\alpha = 03^{\text{h}}04^{\text{m}}13\overset{\text{s}}{.}79$, $\delta = -03^\circ 07' 30\overset{\text{s}}{.}4$ (J2000), classified by

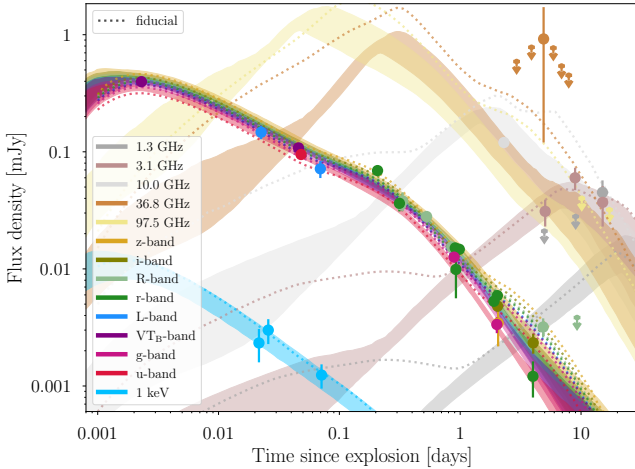


Figure 9. A refreshed shock and two-component structured jet where the second component is a narrow, energetic and baryon-loaded (lower Lorentz factor) sheath that surrounds the rapid core. Shaded regions indicate the 1σ confidence intervals inferred from 250 randomly drawn light curves from the posterior distribution. The x-axis shows the observer time in days and the y-axis the flux density in units of milli-Jansky. The fiducial proof-of-principle model, with parameters listed in the text, is shown as a dotted line. The jet has a refreshed shock episode early in the deceleration, characterised by a collision at ~ 0.05 days in the observer frame. The sheath begins to dominate emission at optical and radio from $\gtrsim 1-2$ days. Sheath emission dominating at later times in this structured jet CSE is due to the larger isotropic equivalent energy within the second component than the jet core.

The Tractor (Lang et al. 2016) as a round exponential source (REX, objid 5790). The location of this candidate host is shown in Fig. 10. The LS DR10 r -band catalogue magnitude is $r_{\text{AB}} = 24.74 \pm 0.36$, corresponding to a marginal detection ($S/N \approx 3$). Its angular separation from the GOTO afterglow position ($\alpha = 03^{\text{h}}04^{\text{m}}13\rlap{.}^{\text{s}}52$, $\delta = -03^{\circ}07'30\rlap{.}''8$) is $R_{\text{off}} = 4\rlap{.}^{\prime}03$. Adopting $z = 1.216$ (from afterglow absorption), this corresponds to a projected physical offset of $R_{\text{off}} = 33.51$ kpc⁶.

To quantify the probability of the host galaxy association to this event, we follow the Bayesian association method of Ackley (2025). In this framework, for a set of N candidate hosts $G = \{G_j\}_{j=1}^N$ within a search region, the probability that G_j is the true host is

$$p(G_j | d) = \frac{p(d | G_j) \pi(G_j)}{\sum_{k=1}^N p(d | G_k) \pi(G_k) + p(d | \emptyset) \pi(\emptyset)}, \quad (2)$$

where d is the GRB afterglow position and redshift, $p(d | G_j)$ is the likelihood, $\pi(G_j)$ is the prior on each galaxy, and $p(d | \emptyset) \pi(\emptyset)$ accounts for the possibility that the true host is not represented by any catalogued object, either because it is outside of the search region or below detection thresholds. We adopt a uniform prior for the N candidates in the search cone, $\pi(G_j) = 1/N$.

The host-association likelihood is factorized into an offset term and a redshift-consistency term,

$$p(d | G_j) = p(r_{\text{DLR}} | G_j) \times p(z | G_j) \equiv p_{\text{offset}}(G_j) \times p_z(G_j), \quad (3)$$

where $r_{\text{DLR}} \equiv \Delta\theta/\text{DLR}$ is the dimensionless host-normalised separation, $\Delta\theta$ is the angular separation between the afterglow and the galaxy centroid, and DLR is the directional light radius of the galaxy

⁶ We assume a flat Λ CDM cosmology with $H_0 = 70 \text{ km s}^{-1} \text{ Mpc}^{-1}$, $\Omega_m = 0.3$, and $\Omega_\Lambda = 0.7$, and quote magnitudes in the AB system unless stated otherwise.

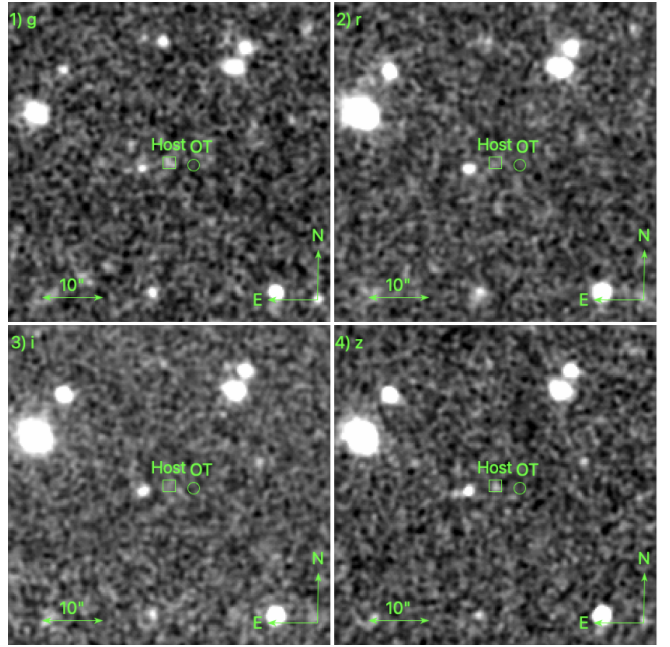


Figure 10. Legacy Survey DR10 image cutouts of the GRB 250818B field in the optical bands: (1) g , (2) r , (3) i , and (4) z . The green circle marks the position of the optical transient (OT), while the green square marks the position of the LS DR10 candidate host galaxy (objid 5790). A faint flux excess is visible at the candidate-host location, most clearly in g , and is less significant in r and i , consistent with the catalogue photometric uncertainties. North and east are indicated, and the scale bar corresponds to $10''$.

in the direction of the afterglow, computed from the galaxy morphology parameters calculated by *the Tractor* Lang et al. (2016).

For the offset likelihood, we marginalise over the unknown true host-normalised offset r_0 as

$$p_{\text{offset}}(G_j) = \sum_c \pi(c) \int_0^\infty p(r_{\text{DLR}} | r_0, \sigma_{r_0}) \pi(r_0 | G_j, c) dr_0, \quad (4)$$

where $c \in \{\text{short, long}\}$ is the class condition. Assuming isotropic 2D Gaussian astrometric uncertainties, the radial likelihood $p(r_{\text{DLR}} | r_0, \sigma_{r_0})$ is a Rice distribution with non-centrality r_0 and scale $\sigma_{r_0} \equiv \sigma_{\text{ast}}/\text{DLR}$. The astrometric error σ_{ast} includes both centroid and registration terms, each conservatively estimated to be on the order of $\sim 0\rlap{.}^{\prime}2$. We note that for the host candidates considered here $\sigma_{r_0} \ll \Delta\theta$, and thus the association is dominated by the offset prior.

We adopt a class-conditional Gamma-family prior to the host-normalised offset

$$\pi(r_0 | c) = \text{Gamma}(r_0; \lambda_c, \kappa_c) \propto r_0^{\lambda_c - 1} \exp(-r_0/\kappa_c) \quad (5)$$

with hyperparameters chosen to reproduce the observed host-normalised offset distributions of short and long GRBs from (Fong et al. 2022a; Blanchard et al. 2016). In our analysis we fix $\lambda_c = 2$ and allow κ_c to vary with class c . To avoid implicitly encoding a progenitor class assumption in our host selection, we search for sources within a large angular radius ($R_{\text{max}} = 0.1^\circ$), for which truncation of the offset prior is negligible for both classes.

For the redshift term, the host galaxy candidates have photometric redshift estimates, while the GRB afterglow has a precise spectroscopic redshift. Therefore, the redshift likelihood $p(z | G_j)$ treats the GRB afterglow redshift as a delta function and the host redshift as a Gaussian with uncertainty given by the photometric red-

shift uncertainty. In practice, this reduces to evaluating the host redshift probability distribution function at the GRB afterglow redshift, $p_z(G_j) \propto p_j(z)$.

In addition to the set of catalogue candidates, the normalisation term of Eq. 2 includes an uncatalogued/missing host term that accounts for the possibility that the true host is not present in the LS DR10 source list. For GRB 250818B, we model this contribution using a limiting-magnitude completeness prescription as implemented in Ackley (2025). We define a catalogue completeness fraction $C(z)$ as the probability that a typical host at $z = 1.216$ would be brighter than the local LS DR10 depth at the burst position. Using the local r -band limiting magnitude m_{lim} (Sec. 3.4.2), we convert to an absolute threshold $M_{\text{lim}} \approx m_{\text{lim}} - \text{DM}(z)$. Given a Schechter luminosity function, we compute $C(z)$ by integrating the galaxy luminosity function above M_{lim} , where

$$C(z) = \frac{\int_{-\infty}^{M_{\text{lim}}} \phi(M) dM}{\int_{-\infty}^{M_{\text{max}}} \phi(M) dM}. \quad (6)$$

The faint/missed host probability is then

$$P_{\text{faint}} = 1 - C(z). \quad (7)$$

We note that we keep $C(z)$ as a term independent of the GRB source type and do not take into consideration any weights to the luminosity function. We also include an outside search cone term that accounts for the fraction of the offset prior that lies beyond the maximum search radius, R_{max} ,

$$P_{\text{out}} = \int_{R_{\text{max}}}^{\infty} p(R) dR. \quad (8)$$

The resulting uncatalogued host term is then approximated as $P_{\emptyset} \approx P_{\text{faint}} + P_{\text{out}}$.

We identify our candidate hosts by querying the LS DR10 catalogue within a 0.1° cone centred on the GRB with the following filters. We select galaxy-like sources with $\text{type} \in \{\text{REX, EXP, DEV, SER}\}$, $\text{brick_primary} = 1$, $\text{allmask_g} = \text{allmask_r} = \text{allmask_z} = 0$, and significant r -band flux ($\text{flux_r} > 0$, $\text{flux_ivar_r} > 0$). For each candidate returned, we calculate the host-association probability, as shown in Table 2.

Given the limiting magnitude of the catalogue, we find that none of the host galaxy candidates in our selection is strongly favoured as the host galaxy. The LS DR10 source (objid 5790) has the highest association probability, $P_{\text{assoc}} = 0.025$, which is primarily driven by the offset likelihood term under a short-GRB offset prior assumption with moderate probabilistic support at the reported photometric redshift of the galaxy. Thus, within the LS DR10 catalogue and in this framework, we cannot definitely identify that objid 5790 is the true host and instead find support for the host being outside of the galaxy catalogue, $P_{\emptyset} \approx 0.882$, where we find that $P_{\text{out}} \approx 0.084$ and $P_{\text{faint}} \approx 0.829$.

We compare our host association probability results against the chance-coincidence formalism of Bloom et al. (2002). The chance-coincidence probability that an unrelated field galaxy of apparent magnitude $\leq m_r$ lies within an angular distance R_{off} of the GRB is

$$P_{\text{cc}} = 1 - \exp[-\pi R_{\text{off}}^2 \sigma(< m_r)], \quad (9)$$

where $\sigma(< m_r)$ is the surface density of galaxies brighter than m_r , in units of arcsec^{-2} . Rather than adopting a generic number-counts model, we measure $\sigma(< m_r)$ directly from the LS DR10 field around GRB 250818B (within 0.1° of the burst position, applying the same catalogue quality and morphology cuts used throughout this work). The resulting cumulative counts $N(< m_r)$, shown in Fig. B4, follow

an approximately log-linear relation with slope $d \log_{10} N/dm_r \simeq 0.32$ over $22.5 \lesssim m_r \lesssim 24.5$, consistent with standard faint galaxy number counts in the R band (e.g. Hogg et al. 1997), but with an overall normalisation lower by a factor of ~ 2.4 relative to that model, likely due to our strict source selection and the limited field size.

At the magnitude of the candidate host ($m_r = 24.74$), the empirical counts imply a surface density of $\sigma(< m_r) \simeq 4.3 \times 10^{-3} \text{ arcsec}^{-2}$ (see Fig. B4), which yields $P_{\text{cc}} \approx 0.195$ (range ≈ 0.18 – 0.20 when propagating the r -band uncertainty). This relatively high P_{cc} reflects the large angular offset and the high surface density of faint galaxies, and implies that the association is tentative rather than definitive. For comparison, using a simple Hogg-like number-counts model normalised to deep R -band surveys would increase P_{cc} to ~ 0.4 ; we adopt the local empirical counts as our baseline, noting that this estimate depends on the chosen field size and the quality/morphology cuts applied to the catalogue.

We also compute P_{cc} for all LS DR10 galaxies in the same 0.1° cone and rank them by increasing chance probability. The LS DR10 object 5790 is among the lowest- P_{cc} galaxies within $\sim 40''$ of the GRB position. The only source with a formally comparable P_{cc} lies at an angular distance of $\simeq 27''$, corresponding to a projected offset of $\simeq 225$ kpc at $z = 1.216$, which is implausibly large for a GRB host (e.g. Mandhai et al. 2022). On this basis, we consider LS DR10 objid 5790 to be a possible host galaxy of GRB 250818B. We caution that the current data do not exclude an even fainter, near-coincident host galaxy candidate below the LS DR10 detection threshold, which would reduce the inferred offset and therefore weaken host-offset-based arguments for a short-GRB classification. We note that P_{cc} quantifies the probability of a chance alignment given only local number counts, whereas the Bayesian framework additionally incorporates host-transient offset priors (via DLR) and redshift consistency; this increases the relative weight of objid 5790 compared to other nearby sources.

To further constrain the redshift of the probable host galaxy, we compare its photometry to the galaxy population in the COSMOS-Web DR1 catalogue (Shuntov et al. 2026). COSMOS-Web DR1 provides photometric redshifts for over 700,000 galaxies in the Cosmic Evolution Survey (COSMOS) field, derived from deep JWST near-infrared imaging combined with extensive HST and ground-based data. In total, 37 photometric bands spanning 0.3 – $8 \mu\text{m}$ are used, yielding some of the most tightly constrained photometric redshifts available for any extragalactic field.

We select COSMOS-Web galaxies whose photometric measurements are consistent with those of the probable host galaxy, requiring agreement within 1σ of the detected fluxes or fainter than the corresponding upper limits. This selection identifies galaxies with photometry compatible with the host, but whose redshifts are constrained by substantially richer multi-wavelength data. The resulting photometric-redshift distribution therefore provides an empirical estimate of the host-galaxy redshift. Using this approach, we obtain a median redshift of $z = 1.118 \pm 0.202$. This result is robust to reasonable variations in the matching criteria (e.g. adopting 3σ rather than 1σ thresholds). Notably, this is close to the measured spectroscopic afterglow redshift.

3.4.2 Limit on an underlying coincident host galaxy candidate

The LS DR10 candidate host galaxy (objid 5790) is offset by $R_{\text{off}} = 4''.03$ from the afterglow position and is detected only marginally in the LS DR10 catalogue ($r_{\text{AB}} = 24.74 \pm 0.36$, $\text{S/N} \approx 3$). Motivated by the relatively large offset and the proximity of the candidate to the survey detection threshold, and noting that the Keck/LRIS

Table 2. Bayesian host-association probability for LS DR10 sources within a 0.1° cone centered on GRB 250818B. The columns list the sky position and morphological type, the host-normalised offset $r_{\text{DLR}} \equiv \Delta\theta/\text{DLR}$, the angular separation from GRB 250818B in units of arcseconds, the projected physical separation at the redshift of GRB 250818B ($z = 1.216$), and the reported redshift of the host with uncertainty ($z_{\text{gal}} \pm \sigma_{z_{\text{gal}}}$). The probability terms represent the offset likelihood P_{offset} , the redshift likelihood P_z , the probability that the host is missing from the catalogue P_\emptyset , and the total probability for the host association P_{assoc} (Eq. 2).

| RA (J2000) | Dec (J2000) | Type | r_{DLR} | Separation ($\Delta\theta, ''$) | Separation (kpc) | $z_{\text{gal}} \pm \sigma_{z_{\text{gal}}}$ | P_{offset} | P_z | P_\emptyset | P_{assoc} |
|----------------------------------------------------|--------------|------|------------------|-----------------------------------|------------------|----------------------------------------------|---------------------|-------|---------------|--------------------|
| 03 ^h 04 ^m 13 ^s 79 | -03°07'30"40 | REX | 15.99 | 4.03 | 33.50 | 1.10 ± 0.32 | 1.000 | 0.752 | 0.882 | 0.025 |
| 03 ^h 04 ^m 14 ^s 08 | -03°07'31"20 | PSF | 14.07 | 8.35 | 69.40 | 0.67 ± 0.41 | 0.013 | 0.538 | 0.882 | 0. |
| 03 ^h 04 ^m 12 ^s 82 | -03°07'26"40 | PSF | 19.08 | 11.32 | 94.06 | 0.75 ± 0.21 | 0. | 0.323 | 0.882 | 0. |
| 03 ^h 04 ^m 13 ^s 08 | -03°07'14"81 | EXP | 20.53 | 17.30 | 143.77 | 0.48 ± 0.07 | 0. | 0.023 | 0.882 | 0. |

spectrum of the afterglow shows metal absorption at the burst redshift (imprinted on the afterglow continuum; Sec. 2.4), we assess whether the current imaging could plausibly miss a fainter, near-coincident host at (or very close to) the afterglow position.

We use the LS DR10 Tractor depth quantities, which are designed to quantify the limiting flux that would have been detected at a given sky position. The LS DR10 catalogues are produced with the TRACTOR image-modelling code (Lang et al. 2016). The `psfdepth_<band>` and `galdepth_<band>` columns encode inverse-variance depth in flux units (nMgy^{-2}), appropriate for point-source and small-galaxy detection, respectively⁷. For an $N\sigma$ detection threshold, the corresponding limiting flux in nanomaggies is $f_{N\sigma} = N/\sqrt{\text{depth}}$, which converts to an AB magnitude via $m_{\text{AB}} = 22.5 - 2.5 \log_{10}(f_{\text{nMgy}})$. We query the LS DR10 Tractor catalogue within a $1'$ radius of the afterglow position and adopt the median depth values in this region as representative of the local detection threshold. For the r band, this yields median depths of $\text{psfdepth}_r \approx 666$ and $\text{galdepth}_r \approx 439 \text{ nMgy}^{-2}$, corresponding to $r_{3\sigma}^{\text{psf}} \approx 24.84$ and $r_{3\sigma}^{\text{gal}} \approx 24.61$ ($r_{5\sigma}^{\text{psf}} \approx 24.28$, $r_{5\sigma}^{\text{gal}} \approx 24.06$). We treat $m_{\text{lim}} \equiv r_{3\sigma}^{\text{gal}}$ as a conservative limit for an underlying host galaxy candidate, and quote $r_{3\sigma}^{\text{psf}}$ as an optimistic (compact-source) case.

As in Section 3.4.1 (Fig. B4), we measure the cumulative surface density $\sigma(< m_r)$ directly from LS DR10 sources in a 0.1° cone around the GRB, selecting galaxy-like morphologies and applying strict quality cuts (`brick_primary`, zero `allmask`, and positive `flux_r` with `flux_ivar_r`). We then evaluate Eq. 9 for a hypothetical host located essentially at the afterglow position by substituting $R_{\text{off}} \rightarrow R_0$ and $m_r \rightarrow m_{\text{lim}}$, where R_0 is a small ‘‘coincident’’ radius. For $R_0 = 0''.5$ (with $0''.3$ in parentheses) and $m_{\text{lim}} = r_{3\sigma}^{\text{gal}} = 24.61$, we obtain

$$P_{\text{cc}}(m_r = m_{\text{lim}}, R_0) \approx 4.2 \times 10^{-3} \quad (1.5 \times 10^{-3}). \quad (10)$$

Adopting the point-source limit $r_{3\sigma}^{\text{psf}} = 24.84$ changes these values only slightly ($\approx 4.3 \times 10^{-3}$ and 1.6×10^{-3} for $R_0 = 0''.5$ and $0''.3$, respectively). Thus, if a host galaxy were present at (or very near) the afterglow position and were bright enough to be detected at the LS DR10 threshold, it would have a very small chance-coincidence probability and would constitute a much stronger association than the offset candidate host.

Conversely, we estimate how faint a near-coincident host galaxy would need to be for its chance-coincidence probability to be comparable to that of the offset candidate ($P_{\text{cc}} \approx 0.24$; Section 3.4.1). Solving Eq. 9 for the required surface density gives

$$\sigma_{\text{req}} = \frac{-\ln(1 - P_{\text{cc}})}{\pi R_0^2}. \quad (11)$$

⁷ <https://www.legacysurvey.org/dr10/catalogs/>

For $P_{\text{cc}} = 0.24$, we obtain $\sigma_{\text{req}} \approx 3.5 \times 10^{-1} \text{ arcsec}^{-2}$ at $R_0 = 0''.5$ ($\sigma_{\text{req}} \approx 9.8 \times 10^{-1} \text{ arcsec}^{-2}$ at $0''.3$). In contrast, our empirical LS DR10 counts in this field reach a maximum of only $\sigma_{\text{max}} \approx 5.7 \times 10^{-3} \text{ arcsec}^{-2}$ by the faintest magnitudes sampled ($r \approx 27.3$). Therefore, the magnitude at which a near-coincident source would attain $P_{\text{cc}} \approx 0.24$ lies far beyond the regime probed by our catalogue (and would require much deeper data), implying that any genuinely near-coincident host would have $P_{\text{cc}} \ll 0.24$.

No galaxy is detected at the afterglow position down to the local LS DR10 limits ($m_{\text{lim}} = r_{3\sigma}^{\text{gal}} \approx 24.61$), so the current data do not exclude a fainter, near-coincident host below the DR10 detection threshold. If present, such a host would reduce the inferred physical offset relative to objid 5790 and weaken offset-based arguments in favour of a short-GRB origin; we discuss the implications further in Section 4.2.

3.4.3 Photometry

We obtained host-galaxy photometry from the DESI Legacy Imaging Surveys DR10 Tractor catalogue (Dey et al. 2019) at the position of the candidate host (Sec. 3.4.1), using DECam *griz* and unWISE/WISE *W1-W4* bands (Flaughier et al. 2015; Dey et al. 2019). Catalogue fluxes and inverse variances were converted to AB magnitudes and 1σ uncertainties following the standard nanomaggy formalism. In the optical, the host galaxy candidate is detected in DECam *g*, *r*, and *z*, while the *i*-band measurement has low signal-to-noise and is treated as an upper limit in our SED fitting. The mid-infrared WISE bands are also of low significance and are used as upper limits only. The LS DR10 Tractor photometry is based on forward modelling of the imaging with PSF convolution, returning band-by-band model fluxes for a common source morphology; we therefore treat the DECam *grz* fluxes as internally consistent total-flux estimates across those bands. The SkyMapper and *WISE* measurements are non-detections and are used only as upper limits; since these limits are substantially shallower than the LS DR10 detections, the SED constraints are dominated by the DECam *grz* points and are insensitive to modest cross-survey aperture/PSF differences. All magnitudes listed in Table A4 are on the AB system and are not corrected for Galactic extinction; for SED modelling we apply the Milky Way extinction corrections described in Sec. 2.2. Given the faintness of the source ($g \approx 24.8$ mag), substantially deeper host imaging and spectroscopy would require large-aperture facilities and lie beyond the scope of this work.

3.4.4 Prospector SED Modelling

We modelled the host galaxy of GRB 250818B with PROSPECTOR (Leja et al. 2017; Johnson et al. 2021), using the FSPS stellar-population models (Conroy et al. 2009; Conroy & Gunn 2010),

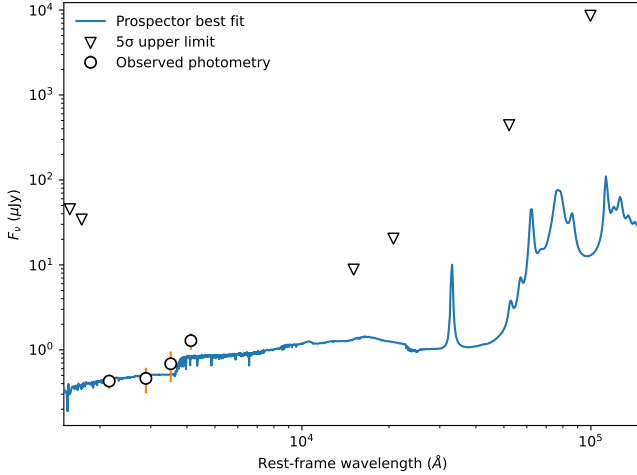


Figure 11. Rest-frame SED of the GRB 250818B host with the PROSPECTOR best-fit spectrum (solid line). Points show DECam *griz* detections (AB, corrected for Galactic extinction); triangles indicate 5σ upper limits (SkyMapper u , v and *WISE* bands). Limited blue/UV and NIR leverage leaves age–dust–metallicity partially degenerate, but the overall SED is well reproduced. The structured emission at $\gtrsim 3 \mu\text{m}$ arises from the model dust/PAH emission component in FSPS/PROSPECTOR; with only upper limits in the mid-IR, this part of the spectrum is effectively unconstrained and is shown for completeness only.

a Chabrier IMF (Chabrier 2003), and a Calzetti foreground dust law (Calzetti et al. 2000). We fix the redshift to $z = 1.216$ from the afterglow absorption spectrum (Fong et al. 2025); therefore, the inferred host properties below are conditional on the assumption that the LS DR10 candidate galaxy is at this redshift (see Sec. 4.2). The star-formation history was modelled with a parametric delayed- τ form. As photometric constraints we used DECam *griz* detections from the DESI Legacy Surveys DR10 Tractor catalogue (Table A4), together with *WISE* $W1$ – $W4$ and SkyMapper u , v non-detections as 5σ upper limits.⁸ As a check, repeating the fit using only the DECam *griz* detections (i.e. omitting the upper-limit bands) yields consistent posteriors for $M_{\star, \text{formed}}$ and A_V . The rest-frame SED fit is shown in Fig. 11; wavelengths are rest-frame unless stated otherwise.

From the posterior, we quote the following physical parameters (medians with 16–84% credible intervals; Fig. 12; see Fig. B5 for the full PROSPECTOR parameter corner plot): $\log(M_{\star, \text{formed}}/M_{\odot}) = 9.77^{+0.31}_{-0.37}$, $\log(Z_{\star}/Z_{\odot}) = -0.19^{+0.25}_{-0.22}$, $A_V = 0.39^{+0.34}_{-0.27}$ mag, and $\log \text{sSFR}_{100 \text{ Myr}} [\text{yr}^{-1}] = -9.28^{+0.47}_{-0.42}$.

The posterior favours a moderate-mass host with modest internal attenuation. In particular, $A_V = 0.39^{+0.34}_{-0.27}$ mag is weakly constrained: the 68% interval spans ~ 0.12 – 0.73 mag, so values consistent with very low attenuation are not excluded, while heavier dust is disfavoured by the blue SED. Given the limited UV/blue and NIR leverage (no deep u/v detection and only mid-IR limits), the age–dust–metallicity degeneracy remains significant and propagates into the posterior uncertainties in $\log Z_{\star}$ and $\text{sSFR}_{100 \text{ Myr}}$. We therefore treat the global host attenuation as small to moderate and avoid using it to draw strong conclusions about the recent ($\lesssim 100$ Myr)

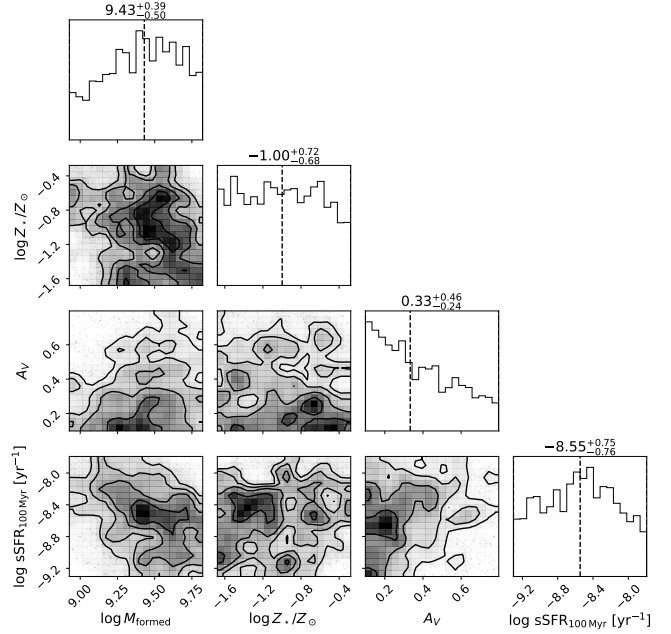


Figure 12. Posterior constraints on derived host properties from the PROSPECTOR fit (Age_{MW} panel omitted). Medians and 68% credible intervals: $\log(M_{\text{formed}}/M_{\odot}) = 9.77^{+0.31}_{-0.37}$, $\log(Z_{\star}/Z_{\odot}) = -0.19^{+0.25}_{-0.22}$, $A_V = 0.39^{+0.34}_{-0.27}$ mag, $\log \text{sSFR}_{100 \text{ Myr}} [\text{yr}^{-1}] = -9.28^{+0.47}_{-0.42}$. The host is consistent with modest attenuation and near-solar metallicity; recent ($\lesssim 100$ Myr) activity remains weakly constrained. For completeness, the full PROSPECTOR parameter corner plot is shown in Fig. B5.

star-formation activity. These inferences are driven primarily by the DECam *griz* detections; deeper UV and a redder/NIR detection (e.g. *YJH*) would substantially tighten the constraints. For completeness, the full PROSPECTOR parameter corner and the SFH summary are shown in Fig. B5 and Fig. B6, respectively.

3.4.5 COSMOS-Web host constraints

As described in Section 3.4.1, we used COSMOS-Web DR1 to place empirical constraints on the redshift of the candidate host by selecting COSMOS-Web galaxies with photometry consistent with the LS DR10 measurements (within the adopted tolerances). We extend the same matching approach to additional physical parameters available for the COSMOS-Web comparison sample. Using the matched galaxies, we infer a typical stellar mass of $\log_{10}(M_{\star}/M_{\odot}) = 9.35 \pm 0.22$ and a typical star-formation rate of $\text{SFR} \approx 1.0 \pm 3.8 M_{\odot} \text{ yr}^{-1}$, corresponding to a median $\log_{10}(\text{sSFR}/\text{yr}^{-1}) \approx -9.34$. These values are consistent with the PROSPECTOR constraints (noting that PROSPECTOR reports a formed stellar mass) at the $\sim 1\sigma$ level. While this COSMOS-Web comparison does not constitute a direct measurement for the specific LS DR10 source, it provides an independent sanity check that the candidate host is plausibly a low-mass galaxy with at most modest ongoing star formation.

4 DISCUSSION

4.1 Afterglow brightness and broadband interpretation

GRB 250818B displays an unusually bright afterglow for a short/Type I event across X-ray, optical, and radio bands. In the observer-frame *Swift*/XRT 0.3–10 keV light curve, it lies on the

⁸ All measurements are AB and were corrected for Galactic extinction using $E(B-V)_{\text{MW}} = 0.0633$ (Schlegel et al. 1998; Schlafly & Finkbeiner 2011) and the band coefficients in Table A3. The upper limits are included in the fit but, given their depth relative to the DECam detections, do not materially impact the inferred posteriors.

bright end of the short-GRB population at early times (Sec. 3.3.1). In the optical, its R-band brightness at ~ 0.3 – 0.9 d is comparable to the median of the overall GRB population, but ~ 2.8 – 3.2 mag brighter than the median of the short/Type I subset (Sec. 3.3.2). In the radio, GRB 250818B is among the most luminous short-GRB afterglows at ($z > 1$) (Sec. 3.3.4). Together, these comparisons indicate that the afterglow emission is bright relative to typical short GRBs, motivating dedicated broadband modelling.

The optical SED at $t_{\text{ref}} = 2.035$ d after the trigger suggests low-to-moderate host-frame dust extinction along the line of sight, $A_V^{\text{host}} \sim 0.2$ mag, with no strong preference between MW- and SMC-like extinction curves (Sec. 3.3.3). The inferred optical spectral index is consistent with the X-ray spectral slope and with a standard slow-cooling synchrotron spectrum, potentially with the cooling break between the optical and X-ray bands (e.g. Sari et al. 1998; Granot & Sari 2002). Thus, the observed optical brightness is unlikely to be dominated by dust obscuration, and the broadband behaviour can be interpreted within the synchrotron afterglow framework.

We modelled the multi-wavelength afterglow using `afterglowpy` (via `redback`) as a baseline forward-shock description. A single-component top-hat jet provides a reasonable overall fit but does not reproduce the full evolution: it exhibits a noticeable mismatch to the X-ray light curve from ~ 0.02 d, underpredicts the optical emission at $\gtrsim 3$ d, and underpredicts the 36.8 GHz detection at ~ 4 – 5 d (noting the large uncertainty on this point). These discrepancies suggest additional structure beyond a simple top-hat forward shock.

Motivated by this behaviour, we explore an energy-injection scenario with a refreshed shock, and a two-component jet model (inner core surrounded by a wider, sheath-like component). In this picture, an early injection episode and a slower, baryon-loaded sheath component surrounding the relativistic core can naturally produce a more complex multi-band evolution, with the sheath contribution becoming important at optical and radio wavelengths from $\gtrsim 1$ – 2 d. Bayesian model comparison prefers the refreshed two-component model over the single-component top-hat fit (Table 1), supporting the interpretation that additional dynamical structure (energy injection and/or angular stratification) is a required feature of this GRB afterglow.

Physically, such energy injection can be produced either by slower ejecta catching up with the decelerating blast wave (refreshed shocks; Rees & Mészáros 1998; Sari & Mészáros 2000) or by sustained power from a long-lived central engine (e.g., magnetar spin-down; Dai & Lu 1998; Zhang & Mészáros 2001; Metzger et al. 2011; Rowlinson et al. 2013), while reverse-shock contributions can further enhance very early optical/radio emission at the afterglow onset (deceleration time, (e.g. Sari & Piran 1999; Kobayashi 2000; Zhang & Kobayashi 2005); as the excess emission is seen at times later than the afterglow peak, we can rule out any reverse shock component for the afterglow variability.

Overall, the broadband brightness of GRB 250818B can be understood as the outcome of one (or more) of the standard levers that control synchrotron afterglow luminosity: higher kinetic energy, a denser circumburst medium, and/or a favourable viewing geometry (e.g. a more on-axis line of sight or a narrow/structured energetic component), potentially augmented by energy injection (e.g. Nakar 2007; Berger 2014). In the baseline fit, relatively high inferred microphysical parameters could also contribute to the flux normalisation; however, these parameters are strongly degenerate with energetics, density, and the location of spectral breaks. In the refreshed two-component model, the microphysics are fixed, and the preference for this model points instead to energy injection and angular structure as a natural explanation for the combination of early-time variabil-

ity and late-time optical/radio excesses. The total isotropic kinetic energy for the refreshed two-component model is $\sim 10^{54}$ erg (after energy injection), with a jet-corrected energy of $E_j \sim 5 \times 10^{51}$ erg – such energetics are approximately two orders of magnitude more energetic than typical short-duration GRBs, and fits more naturally within the long GRB population.

Similar modelling ingredients (energy injection and/or reverse-shock-related components) are commonly invoked to explain the radio behaviour of the most radio-luminous short GRBs, including high-redshift events such as GRB 210726A and GRB 250221A (Sec. 3.3.4; Schroeder et al. 2024, 2025a; Anderson et al. 2025). However, energy injection and/or a two-component jet structure are commonly invoked for long-duration GRBs (e.g., Granot et al. 2003; Sato et al. 2023). In the context of short-duration bursts, GRB 250818B strengthens the emerging picture that the brightest radio afterglows in the short-GRB population may preferentially require departures from the simplest single-component forward-shock description. And in the context of collapsar GRBs, GRB 250818B reinforces the growing evidence for late-time energy injection via refreshed shocks and an energetic wide-angle second component of a structured jet.

GRB 250818B additionally requires an accelerated electron index, $p < 2$, where a value of $p > 2$ typically supports Fermi acceleration at a relativistic shock. A preference for $p < 2$ is often seen, when parameter priors include it or the analysis method does not exclude the $p < 2$ range (e.g., Wang et al. 2015b, where the distribution is found to extend below $p = 2$), and may well indicate that multiple- or alternative particle acceleration mechanisms are at work within the forward shock.

4.2 Host-galaxy association: two viable scenarios

The available imaging and catalogue information admit (at least) two plausible host-galaxy scenarios for GRB 250818B. With the current data, we cannot unambiguously distinguish between them, and we therefore treat the host association as tentative and discuss both possibilities below. We stress that the redshift $z = 1.216$ is derived from metal absorption features imprinted on the afterglow continuum, i.e. material along the GRB sightline, and therefore does not uniquely identify which galaxy (if any) in the LS DR10 imaging is the host. If objid 5790 is the host, the absorption could plausibly arise in its extended circumgalactic medium at projected separations of tens of kpc (e.g. Tumlinson et al. 2017; Nielsen et al. 2013, 2016). Alternatively, it could originate in a fainter, near-coincident host below the LS DR10 detection threshold, or in an unrelated intervening absorber along the line of sight (e.g. Prochter et al. 2006).

Scenario A: the offset LS DR10 galaxy (objid 5790) is the host. In LS DR10 we identify a faint galaxy-like source (objid 5790; $r_{\text{AB}} = 24.74 \pm 0.36$, $\text{S/N} \approx 3$) at an angular separation $R_{\text{off}} = 4.03''$ from the afterglow position (Sec. 3.4.1). At $z = 1.216$, this corresponds to a projected physical offset of ≈ 33.51 kpc. Using the chance-coincidence formalism of Bloom et al. (2002) together with empirical galaxy number counts measured locally from the LS DR10 field (Fig. B4), we obtain a relatively high chance-alignment probability of $P_{\text{cc}} \approx 0.20$, implying that the association is *plausible but not definitive* when judged by angular proximity alone. Nevertheless, we retain objid 5790 as a viable candidate because (i) it is among the lowest- P_{cc} galaxy-like sources in the immediate field at reasonable offsets, and (ii) association information beyond angular proximity (e.g. DLR-based offset priors and redshift consistency) increases its relative weight compared to other nearby catalogued sources within the same framework.

A complementary Bayesian association analysis (Sec. 3.4.1; Ack-

ley 2025) ranks objid 5790 as the most probable host among nearby catalogued sources once additional information is incorporated (e.g. offset priors via DLR and redshift consistency). In addition, an empirical photometric-analogue test using COSMOS-Web DR1 yields a median photometric redshift $z \approx 1.12 \pm 0.20$ for galaxies matched in photometry to the candidate host, consistent with the afterglow absorption redshift within uncertainties (Sec. 3.4.1). We emphasise that this analogue test evaluates whether the *candidate's* photometry is consistent with galaxies at $z \sim 1$; it does not by itself demonstrate that the absorber at $z = 1.216$ is physically associated with objid 5790. We note that if Scenario A is correct, the implied projected offset of $R_{\text{off}} \simeq 33.5$ kpc can provide additional context for the progenitor interpretation; however, we defer any population-based comparison to Sec. 4.3, since offset-based arguments are conditional on the host association being correct.

Scenario B: the true host is a fainter, near-coincident galaxy below the LS DR10 detection threshold. Because objid 5790 lies close to the LS DR10 detection threshold and is substantially offset, the current data do not exclude an undetected host at (or very near) the afterglow position (Sec. 3.4.2). At $z \sim 1.2$, low-luminosity systems can readily fall below the LS DR10 depth, particularly because the observed r band probes the rest-frame near-UV. Using LS DR10 Tractor depth quantities at the GRB position, we estimate local 3σ limits of $r_{3\sigma}^{\text{gal}} \simeq 24.61$ for a small galaxy and $r_{3\sigma}^{\text{psf}} \simeq 24.84$ for a point source (with corresponding 5σ limits $r_{5\sigma}^{\text{gal}} \simeq 24.06$ and $r_{5\sigma}^{\text{psf}} \simeq 24.28$). Combining these limits with the locally measured number counts, a hypothetical coincident host within $R_0 = 0'3 - 0'5$ would have a very small chance-coincidence probability if it were detectable at the LS DR10 threshold, $P_{\text{cc}}(m_{\text{lim}}, R_0) \approx 1.5 \times 10^{-3}$ (for $0'3$) to $\approx 4.2 \times 10^{-3}$ (for $0'5$). No such galaxy is detected at the afterglow position down to these limits, implying that any genuinely near-coincident host must be fainter than LS DR10.

At $z = 1.216$, the LS DR10 r band ($\lambda_{\text{eff}} \sim 6200$ Å) samples the rest-frame near-UV, $\lambda_{\text{rest}} \approx \lambda_{\text{obs}}/(1+z) \simeq 2800$ Å, so translating an observed-frame r -band non-detection into a stellar-mass constraint is highly model dependent (recent star formation and dust can dominate the UV luminosity; e.g. Conroy 2013). In the same manner, the local z -band depth gives $z_{3\sigma}^{\text{gal}} \simeq 23.90$, which corresponds to rest-frame $\lambda_{\text{rest}} \sim 4100$ Å and is therefore somewhat less sensitive to short-timescale UV/SFR variations than r .

Adopting our fiducial cosmology, the distance modulus at $z = 1.216$ is $\mu \simeq 44.63$ mag, so (ignoring the spectral part of the K -correction) these limits correspond to absolute-magnitude *equivalents* at the corresponding rest wavelengths of $M_{2800} \gtrsim r_{3\sigma}^{\text{gal}} - \mu \simeq -20.0$ and $M_{4100} \gtrsim z_{3\sigma}^{\text{gal}} - \mu \simeq -20.7$. For plausible UV-optical spectral slopes, the additional spectral K -correction term is typically of order $\lesssim 1$ mag (e.g. Hogg et al. 2002), so these values should be regarded as order-of-magnitude. Taken at face value, they imply that the current LS DR10 data are sensitive only to relatively luminous galaxies at $z \sim 1.2$, and thus can at best begin to probe the *upper* end of the dwarf-like stellar-mass regime ($M_{\star} \sim 10^7 - 10^9 M_{\odot}$; e.g. Tolstoy et al. 2009; McConnachie 2012; Geha et al. 2012), depending on the assumed SED and mass-to-light ratio. Substantially deeper imaging (e.g. $r \sim 26$ or deeper) would be required to meaningfully test a typical dwarf-mass coincident host at $z \sim 1.2$.

Summary and outlook. In summary, Scenario A is the *best-supported association among catalogued sources* (and is favoured by the Bayesian ranking when DLR priors and redshift consistency are included), but the relatively large P_{cc} and the survey depth mean that Scenario B cannot be ruled out. Accordingly, we do not treat the large projected offset of objid 5790 as decisive evidence on its

own, given the wide offset distribution and host-luminosity diversity in the short-GRB population; if Scenario B holds, the true offset could be small and offset-based classification arguments would be correspondingly weakened. Resolving this ambiguity will require deeper, higher-resolution imaging (to search for a faint coincident host and/or to confirm the morphology and colours of objid 5790) and, ideally, host spectroscopy.

4.3 Progenitor interpretation: merger versus collapsar contamination

Although we adopt the nominal short-GRB classification reported in discovery notices, we note that prompt-duration-based classifications are not definitive, and a non-negligible fraction of apparently short events can arise from collapsars (“short” GRBs drawn from the long/Type II population; e.g. Zhang et al. 2009; Bromberg et al. 2012, 2013). We therefore focus on the afterglow and host-galaxy context, using the extensive multi-wavelength follow-up to assess whether the broadband behaviour is more naturally explained within a compact-object merger (Type I) picture or whether a collapsar origin remains plausible.

Our afterglow modelling (constant-density environment and a preference for energy injection and/or angular structure) does not uniquely distinguish between a compact-object merger and a collapsar origin: similar forward-shock phenomenology and refreshed-shock/engine activity are invoked across both GRB classes, and the inferred circumburst density and energetics are not by themselves decisive (e.g. Woosley & Bloom 2006; Berger 2014). Instead, the most discriminating information in our current dataset is the host association. If Scenario A holds, the implied projected offset of $R_{\text{off}} \simeq 33.51$ kpc would be unusual for a collapsar origin—which is expected to track star-forming regions closely—and would more naturally align with the broad offset distribution of short/Type I GRBs (e.g. Fong et al. 2010, 2013). Conversely, if Scenario B is correct and the burst is associated with a faint, near-coincident host below the LS DR10 detection threshold, then a collapsar origin remains viable and offset-based arguments become correspondingly weaker.

To quantify how unusual the Scenario A offset is in known GRB populations, we compare R_{off} to published distributions of *projected physical offsets* for short and long GRBs (noting that the underlying samples are not population-complete and have different selection functions). For the short-GRB population, we adopt the BRIGHT host catalogue (Fong et al. 2022a) and restrict to the cosmological subset with measured offsets, excluding GRB 170817A (included only as a local point of comparison in Fong et al. 2022a), yielding $N = 83$ events. For our Scenario A offset estimate $R_{\text{off}} = 33.51$ kpc, the empirical tail probability is $f_{\text{short}} = P(R \geq R_{\text{off}}) \simeq 0.108$ (equivalently $\text{CDF}(R_{\text{off}}) \simeq 0.892$). Bootstrap resampling of the $N = 83$ offsets yields a 16–84% range of 0.072–0.145. Thus, an ≈ 33.51 kpc offset lies in the upper tail of the short-GRB offset distribution but remains within the observed short-GRB range (Fig. 13).

In contrast, long GRBs are expected to trace star-forming regions closely, and observed offsets are typically small. Using the *HST*-based long-GRB host sample of Blanchard et al. (2016) and restricting to bursts with measured projected physical offsets ($N = 70$), we find no events with $R_{\text{off}} \geq 33.51$ kpc. For this sample, the corresponding one-sided 95% Clopper–Pearson upper limit is $f_{\text{long}} = P(R \geq R_{\text{off}}) \lesssim 0.0419$. Therefore, if Scenario A is correct, the large projected offset is atypical of the Blanchard et al. (2016) long-GRB host-offset distribution while remaining compatible with the observed short-GRB distribution; if Scenario B holds, however,

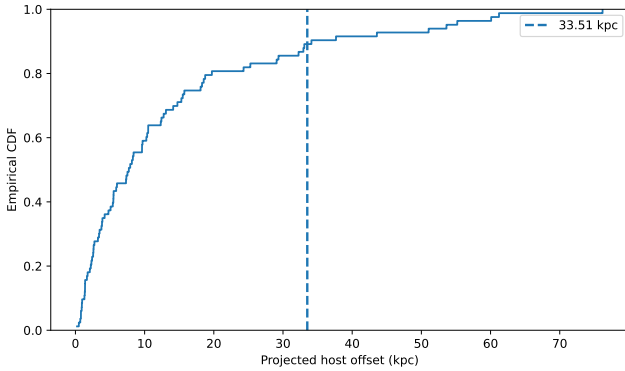


Figure 13. Empirical cumulative distribution of projected (2D) physical offsets for the BRIGHT short-GRB host sample (Fong et al. 2022a), restricted to the cosmological subset with measured offsets ($N = 83$; excluding GRB 170817A as in Fong et al. 2022a). The vertical line indicates the projected offset of GRB 250818B under Scenario A ($R_{\text{off}} = 33.51$ kpc).

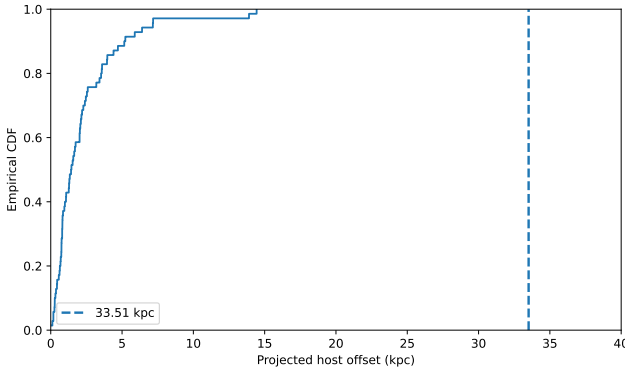


Figure 14. Empirical cumulative distribution of projected physical offsets for the long-GRB host sample of Blanchard et al. (2016), restricted to bursts with measured projected physical offsets ($N = 70$). The vertical line indicates the projected offset of GRB 250818B under Scenario A ($R_{\text{off}} = 33.51$ kpc).

the true physical offset could be small, and this discriminator would not apply.

Additional, non-decisive clues come from the afterglow brightness in the optical and X-ray bands. As shown in Fig. 5, we compare the observer-frame R -band evolution of GRB 250818B to the literature compilation of Kann et al. (2006, 2010, 2011) and the short-GRB sample of Nicuesa Guelbenzu et al. (2012). We show the R -band projection of our simultaneous multiband SBPL fit and place all measurements on a consistent photometric system. Interpolating the comparison light curves in $\log t$ –magnitude space at the epochs of our R -band coverage (0.32, 0.33, 0.53, and 0.85 d), requiring the data to bracket each epoch, we find that GRB 250818B is brighter than ≈ 93 –97% of Type I afterglows ($N_{\text{I}} = 29$ –31). In contrast, it is brighter than ≈ 58 –62% of Type II afterglows ($N_{\text{II}} = 105$ –113), and brighter than ≈ 65 –70% of the combined sample. These percentiles are intended as indicative brightness context (the comparison samples are heterogeneous and not population-complete), but they show that while GRB 250818B lies on the bright tail of the short/Type I afterglow distribution at ~ 0.3 –0.9 d, its optical brightness is broadly typical of the long/Type II population.

A similar conclusion is obtained in X-rays. Building on the population comparison in Section 3.3.1 (Fig. 4), we interpolate UKSSDC

Swift/XRT 0.3–10 keV flux light curves in $\log t$ – $\log F$ space at the three early epochs used for our SNR=10 spectral bins (1869, 2232, and 6153 s), again requiring the data to bracket each epoch and excluding borderline-duration events (defined via BAT T_{90}). At these times, GRB 250818B is brighter than ≈ 96 –99% of the Swift short-duration sample ($N_{\text{short}} = 35$ –47), but brighter than only ≈ 67 –73% of the Swift long-duration sample ($N_{\text{long}} = 994$ –1041). As for the optical comparison, these percentiles are meant as context rather than classification, but they reinforce that GRB 250818B is an outlier among short-GRB afterglows while being comparatively typical of the long-GRB population at similar epochs.

Taken together, the afterglow-brightness context alone does not determine the progenitor class, but it is consistent with either an unusually luminous short-GRB afterglow or a collapsar-contaminated “short” event. Ultimately, the host association remains the strongest discriminator (see Dimple et al. 2025a, for similar conclusions regarding the nominally short GRB 241105A), and deeper, high-resolution imaging and spectroscopy of any putative host would provide the most direct test of the collapsar versus merger interpretations.

5 CONCLUSIONS

We present the discovery and multi-wavelength follow-up of GRB 250818B, a SVOM-triggered burst whose optical afterglow was identified by the wide-field Gravitational-wave Optical Transient Observer (GOTO). We compile and homogenise X-ray, optical/NIR, and radio observations into broadband light curves and spectral energy distributions suitable for physical interpretation, and we investigate both the afterglow physics and the host-galaxy environment. Public prompt-emission constraints are limited, so we adopt the nominal short-GRB classification reported in discovery notices, while our interpretation is driven primarily by the broadband afterglow behaviour and the host-galaxy context.

Keck I/LRIS spectroscopy obtained at ≈ 10.7 hr post-burst reveals a continuum detection with metal absorption features (Fe II, Mg II, Mg I), yielding an absorption redshift of $z = 1.216$ (Fong et al. 2025), which we adopt throughout (Sec. 2.4; Fig. 1). Using *Swift*/XRT data, we performed time-resolved spectral fitting across three independent intervals, and we find that the X-ray afterglow is well described by an absorbed power-law model with a single intrinsic neutral-hydrogen column density (tied between intervals) and a photon index that may vary with time; we find no compelling evidence that more complex spectral models are required.

We constrain dust extinction along the GRB sightline using a host-subtracted optical SED at $t_{\text{ref}} \approx 2.0$ d, constructed from nearly contemporaneous LT *gri* photometry with late-time DECam imaging used to remove the host contribution (Fig. 6). Modelling the SED as a power law attenuated by host-frame dust yields only modest extinction, with $A_V^{\text{host}} = 0.22 \pm 0.18$ mag (Milky Way law) and $A_V^{\text{host}} = 0.20 \pm 0.20$ mag (SMC law), which are statistically indistinguishable and consistent with low extinction within the uncertainties. The inferred optical spectral index is consistent with the XRT-informed prior, supporting a standard synchrotron interpretation at this epoch.

Placing GRB 250818B in context, we compare its afterglow brightness to literature samples and *Swift* GRB populations in the observer frame. The burst lies on the bright end of the *Swift* short-GRB distribution in X-rays at early times (Fig. 4) and is similarly luminous in the optical relative to short/Type I comparison samples at ~ 0.3 –0.9 d (Fig. 5). In the radio, MeerKAT detections at 3.1 GHz (and

later 1.3 GHz), together with deep higher-frequency limits, indicate that GRB 250818B is among the more radio-luminous short-GRB afterglows at $z \gtrsim 1$ in our comparison set.

We model the multi-wavelength afterglow using `afterglowpy` (via `redback`) within the synchrotron forward-shock framework. A single-component top-hat jet provides a reasonable overall description but does not reproduce the full broadband evolution, including mismatches in the X-ray light curve and late-time optical/radio behaviour. Bayesian model comparison favours a refreshed two-component jet scenario (interpretable as energy injection and/or angular structure), supporting the conclusion that departures from the simplest single-component forward shock are required to explain the data (Table 1).

Finally, we investigate the host-galaxy environment and show that the association is non-trivial (Sec. 4.2). The nearest LS DR10 galaxy-like source (Tractor objid 5790; $r_{\text{AB}} = 24.74 \pm 0.36$, $\text{S/N} \approx 3$) lies at an angular separation $R_{\text{off}} = 4''.03$ (≈ 33.51 kpc at $z = 1.216$) and has a relatively high chance-alignment probability, $P_{\text{cc}} \approx 0.20$, implying that the association is plausible but not definitive. A Bayesian host-association analysis following Ackley (2025), which incorporates DLR-normalised offsets and redshift consistency, likewise finds that no catalogued galaxy is strongly favoured: objid 5790 is ranked highest but with only $P_{\text{assoc}} = 0.025$, while the probability that the host is missing from the LS DR10 catalogue is $P_{\emptyset} \approx 0.882$ (dominated by the faint-host term). At the same time, the imaging depth does not exclude a fainter, near-coincident host below the LS DR10 detection threshold, which would reduce the true physical offset and weaken offset-based classification arguments. We emphasise that the redshift $z = 1.216$ is measured from absorption along the GRB sightline and does not, by itself, uniquely identify the host in the available imaging. Conditional on objid 5790 being the host, a COSMOS-Web DR1 photometric-analogue test is also consistent with the candidate lying at $z \sim 1$.

Assuming objid 5790 is the host, SED modelling with PROSPECTOR at fixed $z = 1.216$ yields a moderately low-mass system (formed stellar mass $\log(M_{\star, \text{formed}}/M_{\odot}) \approx 9.77$) with modest attenuation ($A_V \approx 0.39$ mag) and near-solar stellar metallicity ($\log(Z_{\star}/Z_{\odot}) \approx -0.19$; Figs. 11 and 12), albeit with remaining degeneracies due to limited UV/NIR leverage. Overall, GRB 250818B exhibits an unusually bright afterglow for a nominal short GRB across X-ray, optical, and radio bands, enabled by rapid and sustained multi-wavelength follow-up. The homogenised dataset, afterglow modelling, and host-association analysis presented here provide the foundation for interpreting the burst energetics, circumburst environment, and viewing geometry (including possible additional energy supply). Deeper, higher-resolution imaging and host spectroscopy remain essential for resolving host-association ambiguities in high-redshift systems.

ACKNOWLEDGMENTS

The Gravitational-wave Optical Transient Observer (GOTO) project acknowledges the support of the Monash-Warwick Alliance; University of Warwick; Monash University; University of Sheffield; University of Leicester; Armagh Observatory & Planetarium; the National Astronomical Research Institute of Thailand (NARIT); Instituto de Astrofísica de Canarias (IAC); University of Portsmouth; University of Turku; University of Birmingham; and the UK Science and Technology Facilities Council (STFC, grant numbers ST/T007184/1, ST/T003103/1 and ST/Z000165/1). The National Radio Astronomy Observatory and Green Bank Observatory are facilities of the U.S. National Science Foundation operated under cooperative agreement

by Associated Universities, Inc. This paper makes use of the following ALMA data: ADS/JAO.ALMA#2024.1.01131.T. ALMA is a partnership of ESO (representing its member states), NSF (USA) and NINS (Japan), together with NRC (Canada), NSTC and ASIAA (Taiwan), and KASI (Republic of Korea), in cooperation with the Republic of Chile. The Joint ALMA Observatory is operated by ESO, AUI/NRAO and NAOJ. This work made use of data supplied by the UK Swift Science Data Centre at the University of Leicester. This research has made use of data obtained through the High Energy Astrophysics Science Archive Research Center online service, provided by the NASA/Goddard Space Flight Center. W. M. Keck Observatory access was supported by Northwestern University and the Center for Interdisciplinary Exploration and Research in Astrophysics (CIERA). Some of the data presented herein were obtained at the W. M. Keck Observatory, which is operated as a scientific partnership among the California Institute of Technology, the University of California and the National Aeronautics and Space Administration. The Observatory was made possible by the generous financial support of the W. M. Keck Foundation. GPL acknowledges support from the Royal Society (grant Nos. DHF-R1-221175 and DHF-ERE-221005). ACG and the Fong Group at Northwestern acknowledge support by the National Science Foundation under grant Nos. AST-1909358, AST-2206494, AST-2308182 and CAREER grant No. AST-2047919. W. M. Keck Observatory access was supported by Northwestern University and the Center for Interdisciplinary Exploration and Research in Astrophysics (CIERA). MEW is supported by the Science and Technology Facilities Council (STFC). BPG acknowledges support from STFC grant No. ST/Y002253/1. BPG and DO acknowledge support from the Leverhulme Trust grant No. RPG-2024-117. RLCS and SM are supported by Leverhulme Trust grant RPG-2023-240. YS is supported by the Chinese Scholarship Council and the University of Leicester. DMS acknowledges support through the Ramón y Cajal grant RYC2023-044941, funded by MCIN/AEI/10.13039/501100011033 and FSE+. TLK acknowledges support from a Warwick Astrophysics prize post-doctoral fellowship made possible thanks to a generous philanthropic donation. SM acknowledges financial support from the Research Council of Finland project 350458. The authors express their gratitude to the Terskol Observatory Collective Use Center for organizing and making it possible to conduct observations using the Zeiss-2000 telescope of the INASAN observatory.

DATA AVAILABILITY

All data sets supporting this study are provided in the paper. Additional data are available from the corresponding author upon reasonable request.

REFERENCES

- Abbott B. P., et al., 2017, *Phys. Rev. Lett.*, **119**, 161101
- Ackley K., 2025, *arXiv e-prints*, p. arXiv:2510.15836
- Ahumada T., et al., 2022, *ApJ*, **932**, 40
- An J., et al., 2025, GRB Coordinates Network, **41430**, 1
- Anderson G. E., et al., 2024, *ApJ*, **975**, L13
- Anderson G. E., et al., 2025, *ApJ*, **994**, 5
- Angulo-Valdez C., et al., 2025, *arXiv e-prints*, p. arXiv:2510.19132
- Atteia J.-L., et al., 2017, *ApJ*, **837**, 119
- Atteia J.-L., Cordier B., Wei J., 2022, *International Journal of Modern Physics D*, **31**, 2230008
- Barthelmy S. D., et al., 2005, *Space Sci. Rev.*, **120**, 143

Belkin S., et al., 2024, *Research Notes of the American Astronomical Society*, **8**, 6

Berger E., 2014, *ARA&A*, **52**, 43

Berger E., et al., 2005, *Nature*, **438**, 988

Berlato F., Greiner J., Burgess J. M., 2019, *ApJ*, **873**, 60

Blanchard P. K., Berger E., Fong W.-f., 2016, *ApJ*, **817**, 144

Blanton M. R., Roweis S., 2007, *AJ*, **133**, 734

Bloom J. S., Kulkarni S. R., Djorgovski S. G., 2002, *AJ*, **123**, 1111

Breeveld A. A., Landsman W., Holland S. T., Roming P., Kuin N. P. M., Page M. J., 2011, in McEnery J. E., Racusin J. L., Gehrels N., eds, American Institute of Physics Conference Series Vol. 1358, Gamma Ray Bursts 2010. AIP, pp 373–376 ([arXiv:1102.4717](https://arxiv.org/abs/1102.4717)), doi:10.1063/1.3621807

Broe Bendtsen J., et al., 2025, GRB Coordinates Network, **41426**, 1

Bromberg O., Nakar E., Piran T., Sari R., 2012, *ApJ*, **749**, 110

Bromberg O., Nakar E., Piran T., Sari R., 2013, *ApJ*, **764**, 179

Burgess J. M., Yu H.-F., Greiner J., Mortlock D. J., 2018, *MNRAS*, **476**, 1427

Burrows D. N., et al., 2005, *Space Sci. Rev.*, **120**, 165

Busmann M., Fabà J., Jain V., Zuo X., Gruen D., O'Connor B., Palmese A., 2025, GRB Coordinates Network, **41445**, 1

Calzetti D., Armus L., Bohlin R. C., Kinney A. L., Koornneef J., Storchi-Bergmann T., 2000, *ApJ*, **533**, 682

Cano Z., Wang S.-Q., Dai Z.-G., Wu X.-F., 2017, *Advances in Astronomy*, **2017**, 8929054

Cao Z., et al., 2023, *Science Advances*, **9**, eadj2778

Cash W., 1979, *ApJ*, **228**, 939

Castrejon C., Nugent A. E., Fong W.-f., Schroeder G., Rouco Escorial A., Guerra O., 2025, *arXiv e-prints*, p. [arXiv:2508.20156](https://arxiv.org/abs/2508.20156)

Chabrier G., 2003, *PASP*, **115**, 763

Chandra P., Frail D. A., 2012, *ApJ*, **746**, 156

Chastain S. I., et al., 2024, *MNRAS*, **532**, 2820

Connaughton V., et al., 2015, *ApJS*, **216**, 32

Conroy C., 2013, *ARA&A*, **51**, 393

Conroy C., Gunn J. E., 2010, *ApJ*, **712**, 833

Conroy C., Gunn J. E., White M., 2009, *ApJ*, **699**, 486

Dai Z. G., Lu T., 1998, *A&A*, **333**, L87

Dai C.-Y., Guo C.-L., Zhang H.-M., Liu R.-Y., Wang X.-Y., 2024, *ApJ*, **962**, L37

Dey A., et al., 2019, *AJ*, **157**, 168

Dimple et al., 2025a, *MNRAS*, **544**, 548

Dimple Gompertz B. P., Kumar A., 2025b, GRB Coordinates Network, **41442**, 1

Dyer M. J., et al., 2024, in Marshall H. K., Spyromilio J., Usuda T., eds, Society of Photo-Optical Instrumentation Engineers (SPIE) Conference Series Vol. 13094, Ground-based and Airborne Telescopes X. p. 130941X ([arXiv:2407.17176](https://arxiv.org/abs/2407.17176)), doi:10.11117/12.3018305

Eichler D., Livio M., Piran T., Schramm D. N., 1989, *Nature*, **340**, 126

Evans P. A., et al., 2009, *MNRAS*, **397**, 1177

Ferro M., et al., 2025, GRB Coordinates Network, **41407**, 1

Fitzpatrick E. L., 1999, *PASP*, **111**, 63

Fitzpatrick E. L., Massa D., 2007, *ApJ*, **663**, 320

Flaugher B., et al., 2015, *AJ*, **150**, 150

Fong W., Berger E., 2013, *ApJ*, **776**, 18

Fong W., Berger E., Fox D. B., 2010, *ApJ*, **708**, 9

Fong W., et al., 2013, *ApJ*, **769**, 56

Fong W., et al., 2014, *ApJ*, **780**, 118

Fong W., Berger E., Margutti R., Zauderer B. A., 2015, *ApJ*, **815**, 102

Fong W., et al., 2021, *ApJ*, **906**, 127

Fong W.-f., et al., 2022a, *ApJ*, **940**, 56

Fong W.-f., et al., 2022b, *ApJ*, **940**, 56

Fong W., Gordon A. C., Levan A. J., Tanvir N. R., Dong Y., Suresh A., Liu C., 2025, GRB Coordinates Network, **41419**, 1

Galáma T. J., et al., 1998, *Nature*, **395**, 670

Geha M., Blanton M. R., Yan R., Tinker J. L., 2012, *ApJ*, **757**, 85

Goldstein A., et al., 2017, *ApJ*, **848**, L14

Gompertz B. P., et al., 2023, *Nature Astronomy*, **7**, 67

Gordon K., 2024, *The Journal of Open Source Software*, **9**, 7023

Gordon K. D., Clayton G. C., Misselt K. A., Landolt A. U., Wolff M. J., 2003, *ApJ*, **594**, 279

Granot J., Sari R., 2002, *ApJ*, **568**, 820

Granot J., Nakar E., Piran T., 2003, *Nature*, **426**, 138

Gulati A., Anderson G. E., Morley C., Chastain S., Leung J. K., van der Horst A. J., Rhodes L., ATCA PanRadio GRB Collaboration 2025, GRB Coordinates Network, **39501**, 1

Heintz K. E., et al., 2020, *ApJ*, **903**, 152

Hellot R., et al., 2025, GRB Coordinates Network, **41444**, 1

Hennessy A., et al., 2025, *MNRAS*, **544**, 53

Hjorth J., et al., 2003, *Nature*, **423**, 847

Hogg D. W., Pahre M. A., McCarthy J. K., Cohen J. G., Blandford R., Smail I., Soifer B. T., 1997, *MNRAS*, **288**, 404

Hogg D. W., Baldry I. K., Blanton M. R., Eisenstein D. J., 2002, *arXiv e-prints*, pp [astro-ph/0210394](https://arxiv.org/abs/astro-ph/0210394)

Johnson B. D., Leja J., Conroy C., Speagle J. S., 2021, *ApJS*, **254**, 22

Kann D. A., Klose S., Zeh A., 2006, *ApJ*, **641**, 993

Kann D. A., et al., 2010, *ApJ*, **720**, 1513

Kann D. A., et al., 2011, *ApJ*, **734**, 96

Klebesadel R. W., Strong I. B., Olson R. A., 1973, *ApJ*, **182**, L85

Kobayashi S., 2000, *ApJ*, **545**, 807

Kouveliotou C., Meegan C. A., Fishman G. J., Bhat N. P., Briggs M. S., Koshut T. M., Paciesas W. S., Pendleton G. N., 1993, *ApJ*, **413**, L101

Kumar P., Zhang B., 2015, *Phys. Rep.*, **561**, 1

Kumar A., et al., 2024, *MNRAS*, **531**, 3297

Kumar A., et al., 2025a, *MNRAS*, **544**, 1541

Kumar A., et al., 2025b, Transient Name Server Discovery Report, **2025-3254**, 1

Kumar A., et al., 2025c, GRB Coordinates Network, **41406**, 1

Kumar A., et al., 2025d, GRB Coordinates Network, **41431**, 1

Kumar A., et al., 2025e, GRB Coordinates Network, **41431**, 1

Lamb G. P., Kobayashi S., 2017, *MNRAS*, **472**, 4953

Lamb G. P., Mandel I., Resmi L., 2018, *MNRAS*, **481**, 2581

Lamb G. P., et al., 2019, *ApJ*, **883**, 48

Lamb G. P., Levan A. J., Tanvir N. R., 2020, *ApJ*, **899**, 105

Lang D., Hogg D. W., Myktyyn D., 2016, The Tractor: Probabilistic astronomical source detection and measurement, *Astrophysics Source Code Library*, record ascl:1604.008 (ascl:1604.008)

Laskar T., et al., 2022, *ApJ*, **935**, L11

Lazzati D., Perna R., Gompertz B. P., Levan A. J., 2023, *ApJ*, **950**, L20

Leja J., Johnson B. D., Conroy C., van Dokkum P. G., Byler N., 2017, *ApJ*, **837**, 170

Levan A. J., et al., 2023, *Nature Astronomy*, **7**, 976

Levan A. J., et al., 2024, *Nature*, **626**, 737

Li R.-Z., Fu Y.-C., Zhang W.-D., Liu Y., Einstein Probe Team 2025, GRB Coordinates Network, **41424**, 1

Lien A., et al., 2016, *ApJ*, **829**, 7

López K. O. C., Watson A. M., Lee W. H., Becerra R. L., Pereyra M., 2024, *MNRAS*, **531**, 2775

Mandhai S., Lamb G. P., Tanvir N. R., Bray J., Nixon C. J., Eyles-Ferris R. A. J., Levan A. J., Gompertz B. P., 2022, *MNRAS*, **514**, 2716

McConnachie A. W., 2012, *AJ*, **144**, 4

Meegan C., et al., 2009, *ApJ*, **702**, 791

Metzger B. D., Giannios D., Thompson T. A., Bucciantini N., Quataert E., 2011, *MNRAS*, **413**, 2031

Miceli D., Nava L., 2022, *Galaxies*, **10**, 66

Mong Y.-L., et al., 2021, *MNRAS*, **507**, 5463

Moskvitin A., Spiridonova O., Vlasysk V., Sotnikova Y., An T., Liu Y., 2025, GRB Coordinates Network, **41428**, 1

Nakar E., 2007, *Phys. Rep.*, **442**, 166

Narayan R., Paczynski B., Piran T., 1992, *ApJ*, **395**, L83

Nayana A. J., Chandra P., 2014, GRB Coordinates Network, **16815**, 1

Nicuesa Guelbenzu A., et al., 2012, *A&A*, **548**, A101

Nielsen N. M., Churchill C. W., Kacprzak G. G., 2013, *ApJ*, **776**, 115

Nielsen N. M., Churchill C. W., Kacprzak G. G., Murphy M. T., Evans J. L., 2016, *ApJ*, **818**, 171

Nousek J. A., et al., 2006, *ApJ*, **642**, 389

Nugent A. E., Fong W.-f., Castrejon C., Leja J., Zevin M., Ji A. P., 2024, *ApJ*, **962**, 5

O'Connor B., et al., 2023, *Science Advances*, **9**, eadi1405

Oke J. B., Gunn J. E., 1983, *ApJ*, **266**, 713
 Oke J. B., et al., 1995, *PASP*, **107**, 375
 Panaiteescu A., 2006, *MNRAS*, **367**, L42
 Panaiteescu A., Kumar P., 2002, *ApJ*, **571**, 779
 Pe'er A., 2024, *Galaxies*, **13**, 2
 Pian E., et al., 2017, *Nature*, **551**, 67
 Piran T., 2004, *Reviews of Modern Physics*, **76**, 1143
 Poole T. S., et al., 2008, *MNRAS*, **383**, 627
 Prochaska J. X., et al., 2020a, pypeit/PypeIt: Release 1.0.0, doi:10.5281/zenodo.3743493
 Prochaska J., et al., 2020b, *The Journal of Open Source Software*, **5**, 2308
 Prochter G. E., et al., 2006, *ApJ*, **648**, L93
 Rastinejad J. C., et al., 2022, *Nature*, **612**, 223
 Rees M. J., Mészáros P., 1998, *ApJ*, **496**, L1
 Rhoads J. E., 1999, *ApJ*, **525**, 737
 Ricci R., Becerra R. L., Troja E., ERC BHianca Team 2025a, GRB Coordinates Network, **41046**, 1
 Ricci R., Yadav M., Troja E., 2025b, GRB Coordinates Network, **41455**, 1
 Roming P. W. A., et al., 2005, *Space Sci. Rev.*, **120**, 95
 Rossi A., et al., 2022, *ApJ*, **932**, 1
 Rowlinson A., O'Brien P. T., Metzger B. D., Tanvir N. R., Levan A. J., 2013, *MNRAS*, **430**, 1061
 Rowlinson A., et al., 2024, *MNRAS*, **534**, 2592
 Ryan G., van Eerten H., Piro L., Troja E., 2020, *ApJ*, **896**, 166
 Sari R., Mészáros P., 2000, *ApJ*, **535**, L33
 Sari R., Piran T., 1999, *ApJ*, **520**, 641
 Sari R., Piran T., Narayan R., 1998, *ApJ*, **497**, L17
 Sarin N., et al., 2024, *MNRAS*, **531**, 1203
 Sato Y., Murase K., Ohira Y., Yamazaki R., 2023, *MNRAS*, **522**, L56
 Savchenko V., et al., 2017, *ApJ*, **848**, L15
 Schlaflay E. F., Finkbeiner D. P., 2011, *ApJ*, **737**, 103
 Schlegel D. J., Finkbeiner D. P., Davis M., 1998, *ApJ*, **500**, 525
 Schroeder G., et al., 2024, *ApJ*, **970**, 139
 Schroeder G., et al., 2025a, *ApJ*, **982**, 42
 Schroeder G., Rhodes L., Fong W., Levan A. J., 2025b, GRB Coordinates Network, **40546**, 1
 Schroeder G., Rhodes L., Fong W., Laskar T., Berger E., 2025c, GRB Coordinates Network, **41060**, 1
 Schroeder G., Fong W., Laskar T., Rhodes L., 2025d, GRB Coordinates Network, **41516**, 1
 Shuntov M., et al., 2026, *A&A*, **704**, A339
 Siegel M. H., Swift/UVOT Team 2025, GRB Coordinates Network, **41435**, 1
 Singer L. P., et al., 2015, *ApJ*, **806**, 52
 Soderberg A. M., et al., 2006, *ApJ*, **650**, 261
 Steeghs D., et al., 2022, *MNRAS*, **511**, 2405
 Stratta G., et al., 2025, *ApJ*, **979**, 159
 Sun H., et al., 2025, *National Science Review*, **12**, nwae401
 Takahashi K., Ioka K., 2021, *MNRAS*, **501**, 5746
 Tanaka M., 2016, *Advances in Astronomy*, **2016**, 634197
 Tanvir N. R., et al., 2017, *ApJ*, **848**, L27
 Tolstoy E., Hill V., Tosi M., 2009, *ARA&A*, **47**, 371
 Troja E., et al., 2017, *Nature*, **551**, 71
 Troja E., et al., 2022, *Nature*, **612**, 228
 Tumlinson J., Peeples M. S., Werk J. K., 2017, *ARA&A*, **55**, 389
 Turpin D., Heussaff V., Dezalay J.-P., Atteia J.-L., Klotz A., Dornic D., 2016, *ApJ*, **831**, 28
 Valenti S., et al., 2017, *ApJ*, **848**, L24
 Virtanen P., et al., 2020, *Nature Medicine*, **17**, 261
 Volvach A., Volvach L., Larionov M., 2025, *ApJ*, **992**, 60
 Wang F. Y., Dai Z. G., Liang E. W., 2015a, *New Astron. Rev.*, **67**, 1
 Wang X.-G., et al., 2015b, *ApJS*, **219**, 9
 Wang H., et al., 2017, *ApJ*, **851**, L18
 Wang Z. Q., Liang Y. F., Xie W. J., Zhao D. H., Robinet F., Zhang L., SVOM mission Team 2025, GRB Coordinates Network, **41405**, 1
 Wei J., et al., 2016, *arXiv e-prints*, p. arXiv:1610.06892
 Williams P. K. G., Clavel M., Newton E., Ryzhkov D., 2017, pwkit: Astronomical utilities in Python, *Astrophysics Source Code Library*, record ascl:1704.001 (ascl:1704.001)

Williams M. J., Veitch J., Messenger C., 2021, *Phys. Rev. D*, **103**, 103006
 Williams M. J., Veitch J., Messenger C., 2023, *Machine Learning: Science and Technology*, **4**, 035011
 Willingale R., Starling R. L. C., Beardmore A. P., Tanvir N. R., O'Brien P. T., 2013, *MNRAS*, **431**, 394
 Wilms J., Allen A., McCray R., 2000, *ApJ*, **542**, 914
 Woosley S. E., Bloom J. S., 2006, *ARA&A*, **44**, 507
 Yang J., et al., 2022, *Nature*, **612**, 232
 Yao Z. H., et al., 2025, GRB Coordinates Network, **41409**, 1
 Yi F., Haibo Y., Ruoyi Z., Jian G., Shuai X., 2023, *MNRAS*, **525**, 2701
 Yuan W., et al., 2015, *arXiv e-prints*, p. arXiv:1506.07735
 Zhang B., Kobayashi S., 2005, *ApJ*, **628**, 315
 Zhang B., Mészáros P., 2001, *ApJ*, **552**, L35
 Zhang B., Mészáros P., 2002, *ApJ*, **571**, 876
 Zhang B., Kobayashi S., Mészáros P., 2003, *ApJ*, **595**, 950
 Zhang B., et al., 2009, *ApJ*, **703**, 1696
 Zhang B.-B., et al., 2021, *Nature Astronomy*, **5**, 911
 Zheng W., Han X., Zhang P., Filippenko A. V., KAIT GRB team 2025, GRB Coordinates Network, **41417**, 1
 von Kienlin A., et al., 2020, *ApJ*, **893**, 46

APPENDIX A: DATA TABLES

Table A1: Optical and near-infrared afterglow observations of GRB 250818B compiled in this work, including measurements reported in GCN Circulars. All magnitudes are in the AB system. Upper limits are 3σ and are indicated with a ">" sign. Times are measured relative to the *SVOM/ECLAIRs* trigger at $T_0 = 2025-08-18T03:29:09$ UTC.

| $T - T_0$ (h) | Instrument/Telescope | Exp. Time (s) | Filter | Mag | Mag err | Source |
|---------------|----------------------|-----------------|-------------|---------|---------|-----------------------------------------------------|
| -9.23 | GOTO-S | 4×45 | <i>L</i> | > 20.3 | | This work |
| 0.06 | SVOM/VT | 50 | <i>VT_B</i> | 17.40 | 0.03 | Yao et al. (2025) |
| 0.54 | GOTO | 4×90 | <i>L</i> | 18.48 | 0.14 | This work |
| 1.10 | SVOM/VT | 50 | <i>VT_B</i> | 18.81 | 0.03 | Yao et al. (2025) |
| 1.16 | Swift/UVOT | 1544 | <i>u</i> | 18.96 | 0.06 | Siegel & Swift/UVOT Team (2025) |
| 1.67 | GOTO | 4×90 | <i>L</i> | 19.26 | 0.18 | This work |
| 4.97 | KNC/CDK17-AITP | 15×300 | <i>r</i> | 19.30 | 0.07 | Hellot et al. (2025) |
| 7.53 | KNC/TEC160FL | 11×300 | <i>r</i> | 20.00 | 0.16 | Hellot et al. (2025) |
| 7.75 | TRT/0.7m | – | <i>R</i> | 20.03 | 0.06 | An et al. (2025) |
| 8.00 | KAIT | 90×60 | <i>R</i> | 19.95 | 0.20 | Zheng et al. (2025) |
| 12.64 | TRT/0.7m | – | <i>R</i> | 20.28 | 0.06 | An et al. (2025) |
| 20.42 | SAO RAS/Zeiss-1000 | 13×300 | <i>R</i> | 20.93 | 0.04 | Moskvitin et al. (2025) |
| 21.37 | SAAO/1mLesedi | 6×450 | <i>g'</i> | 21.15 | 0.09 | Kumar et al. (2025e) |
| 21.84 | FTW/3KK | 35×180 | <i>r</i> | 20.95 | 0.02 | Busmann et al. (2025) |
| 22.13 | SAAO/1mLesedi | 6×400 | <i>r'</i> | 21.41 | 0.47 | Kumar et al. (2025e) |
| 23.60 | NOT/ALFOSC | 3×300 | <i>r</i> | 20.98 | 0.04 | Broe Bendtsen et al. (2025) |
| 45.60 | FTW/3KK | 30×180 | <i>r</i> | 22.09 | 0.08 | Busmann et al. (2025) |
| 48.24 | LT/IO:O | | <i>g</i> | 22.59 | 0.17 | This work |
| 48.72 | LT/IO:O | 5×240 | <i>r</i> | 21.97 | 0.10 | Dimple et al. (2025b) |
| 48.96 | LT/IO:O | | <i>i</i> | 22.19 | 0.11 | This work |
| 49.44 | LT/IO:O | | <i>z</i> | 22.56 | 0.40 | This work |
| 96.00 | LT/IO:O | | <i>r</i> | 23.69 | 0.37 | This work |
| 96.48 | LT/IO:O | | <i>i</i> | 22.97 | 0.21 | This work |
| 116.59 | Terskol/Zeiss-2000 | 3420 | <i>R</i> | 22.64 | 0.20 | This work |
| 222.55 | Terskol/Zeiss-2000 | 3720 | <i>R</i> | > 22.44 | | This work |

Table A2. Vega-to-AB magnitude offsets Δm adopted in this work, defined such that $m_{\text{AB}} = m_{\text{Vega}} + \Delta m$.

| Filter | Photometric system | $\Delta m = m_{\text{AB}} - m_{\text{Vega}}$ |
|----------------------|--------------------|----------------------------------------------|
| <i>U</i> | Johnson–Cousins | 0.79 |
| <i>B</i> | Johnson–Cousins | −0.09 |
| <i>V</i> | Johnson–Cousins | 0.02 |
| <i>R</i> | Johnson–Cousins | 0.21 |
| <i>I</i> | Johnson–Cousins | 0.45 |
| <i>J</i> | NIR (2MASS-like) | 0.91 |
| <i>H</i> | NIR (2MASS-like) | 1.39 |
| <i>K_s</i> | NIR (2MASS-like) | 1.85 |
| <i>g</i> | Sloan-like | −0.08 |
| <i>r</i> | Sloan-like | 0.16 |
| <i>i</i> | Sloan-like | 0.37 |
| <i>z</i> | Sloan-like | 0.54 |
| <i>u</i> | <i>Swift</i> /UVOT | 1.02 |
| <i>b</i> | <i>Swift</i> /UVOT | −0.13 |
| <i>v</i> | <i>Swift</i> /UVOT | 0.00 |

Table A3. Milky Way extinction coefficients $A_\lambda/E(B-V)$ adopted in this work.

| Filter | Origin | $A_\lambda/E(B-V)$ |
|------------------------------|--------------------------------------------------|-----------------------------|
| <i>g</i> (SDSS-like) | Schlafly & Finkbeiner (2011) | 3.303 |
| <i>r</i> (SDSS-like) | Schlafly & Finkbeiner (2011) | 2.285 |
| <i>i</i> (SDSS-like) | Schlafly & Finkbeiner (2011) | 1.698 |
| <i>z</i> (SDSS-like) | Schlafly & Finkbeiner (2011) | 1.263 |
| <i>U</i> (Landolt) | Fitzpatrick (1999) | 4.334 |
| <i>B</i> (Landolt) | Fitzpatrick (1999) | 3.626 |
| <i>V</i> (Landolt) | Fitzpatrick (1999) | 2.742 |
| <i>R</i> (Landolt) | Fitzpatrick (1999) | 2.169 |
| <i>I</i> (Landolt) | Fitzpatrick (1999) | 1.505 |
| <i>u</i> (UVOT) ^c | Yi et al. (2023) | 4.80 |
| <i>b</i> (UVOT) ^c | Yi et al. (2023) | 3.97 |
| <i>v</i> (UVOT) ^c | Yi et al. (2023) | 2.99 |
| <i>L</i> (GOTO) | this work ^a | $0.997 R_V \simeq 3.09$ |
| VT _B (SVOM) | this work ^b | $(A_g + A_r)/2 \simeq 2.79$ |

^a Approximated as $A_L \simeq 0.997 A_V$ with $R_V = 3.1$.

^b Approximated as the mean of the SDSS *g* and *r* coefficients.

^c UVOT coefficients are taken from [Yi et al. \(2023\)](#) and are tabulated per $E(B-V)$ from the SFD98 map ([Schlegel et al. 1998](#)). Since we adopt the [Schlafly & Finkbeiner \(2011\)](#) recalibration

$E(B-V)_{\text{SF11}} \approx 0.0633 E(B-V)_{\text{SFD}}$ ([Schlafly & Finkbeiner 2011](#)), we rescale the UVOT coefficients by $1/0.0633$ so that $A_\lambda/E(B-V)$ is consistent with our adopted $E(B-V)$.

Table A4. Host-galaxy photometry at the position of GRB 250818B, from the DESI Legacy Imaging Surveys DR10 Tractor catalogue (DECam *griz*) and WISE (*W1*–*W4*). All magnitudes are AB and are not corrected for Galactic extinction. For bands with low signal-to-noise, we quote 3σ upper limits.

| Band | Instrument | m_{AB} | err |
|-----------|------------|-----------------|------|
| <i>u</i> | SkyMapper | > 19.76 | |
| <i>v</i> | SkyMapper | > 20.07 | |
| <i>g</i> | DECam | 24.82 | 0.20 |
| <i>r</i> | DECam | 24.74 | 0.36 |
| <i>i</i> | DECam | 24.31 | 0.43 |
| <i>z</i> | DECam | 23.63 | 0.24 |
| <i>W1</i> | WISE | > 21.54 | |
| <i>W2</i> | WISE | > 20.63 | |
| <i>W3</i> | WISE | > 17.29 | |
| <i>W4</i> | WISE | > 14.07 | |

Table A5. Radio observations of GRB 250818B. Upper limits are 3σ .

| Facility | Frequency (GHz) | $T - T_0$ (d) | Flux density (μ Jy) | Flux err (μ Jy) | Source |
|----------|-----------------|---------------|--------------------------|----------------------|--------------------------------------|
| VLA | 10.0 | 2.30 | 120 | | Ricci et al. (2025b) |
| MeerKAT | 1.3 | 4.97 | <21 | | This Work |
| MeerKAT | 1.3 | 9.02 | <28 | | This Work |
| MeerKAT | 1.3 | 15.05 | 45 | 12 | This Work |
| MeerKAT | 1.3 | 32.00 | <18 | | This Work |
| MeerKAT | 3.1 | 5.05 | 31 | 8 | This Work |
| MeerKAT | 3.1 | 8.93 | 60 | 13 | This Work |
| MeerKAT | 3.1 | 15.1 | 37 | 14 | This Work |
| MeerKAT | 3.1 | 32.1 | <32 | | This Work |
| CrAO | 36.8 | 2.93 | < 590 | | This work |
| CrAO | 36.8 | 3.89 | < 780 | | This work |
| CrAO | 36.8 | 4.90 | 920 | 800 | This work |
| CrAO | 36.8 | 5.90 | < 770 | | This work |
| CrAO | 36.8 | 6.90 | < 540 | | This work |
| CrAO | 36.8 | 7.91 | < 450 | | This work |
| ALMA | 97.5 | 10.14 | < 40 | | This work |
| ALMA | 97.5 | 17.19 | < 32 | | This work |

Table A6. *Swift*/XRT 0.3-10 keV fluxes of GRB 250818B (SNR = 10 binning). The best-fit hydrogen absorption is N_{H} (intrinsic) = $(2.09^{+2.51}_{-2.09}) \times 10^{21} \text{ cm}^{-2}$, consistent with no excess above the galactic value of $6.49 \times 10^{20} \text{ cm}^{-2}$ ([Willingale et al. 2013](#)). The reduced fit statistic is 0.24. All errors are to the 90% tolerance level.

| Bin Centroid (s) | Bin Width (s) | Absorbed Flux ($10^{-11} \text{ erg cm}^{-2} \text{ s}^{-1}$) | Unabsorbed Flux ($10^{-11} \text{ erg cm}^{-2} \text{ s}^{-1}$) | Photon Index |
|------------------|---------------|-----------------------------------------------------------------|-------------------------------------------------------------------|------------------------|
| 1869 | 371.1 | $2.58^{+0.55}_{-0.45}$ | $2.91^{+0.51}_{-0.43}$ | $1.64^{+0.23}_{-0.22}$ |
| 2232 | 355.3 | $2.82^{+0.51}_{-0.42}$ | $3.32^{+0.48}_{-0.42}$ | $1.84^{+0.22}_{-0.21}$ |
| 6153 | 837.4 | $0.96^{+0.16}_{-0.14}$ | $1.25^{+0.18}_{-0.16}$ | $2.19^{+0.24}_{-0.23}$ |

Table A7. *Swift*/XRT 0.3-10 keV fluxes of GRB 250818B (SNR = 5 binning). The best-fit hydrogen absorption is N_{H} (intrinsic) = $(0.79^{+2.21}_{-0.79}) \times 10^{21} \text{ cm}^{-2}$, consistent with no excess above the galactic value of $6.49 \times 10^{20} \text{ cm}^{-2}$ ([Willingale et al. 2013](#)). The reduced fit statistic is 0.12. All errors are to the 90% tolerance level.

| Bin Centroid (s) | Bin Width (s) | Absorbed Flux ($10^{-11} \text{ erg cm}^{-2} \text{ s}^{-1}$) | Unabsorbed Flux ($10^{-11} \text{ erg cm}^{-2} \text{ s}^{-1}$) | Photon Index |
|------------------|---------------|-----------------------------------------------------------------|-------------------------------------------------------------------|------------------------|
| 1745 | 122.9 | $2.51^{+0.82}_{-0.58}$ | $2.97^{+0.76}_{-0.65}$ | $1.94^{+0.35}_{-0.34}$ |
| 1892 | 170.5 | $2.05^{+0.48}_{-0.38}$ | $2.33^{+0.46}_{-0.38}$ | $1.79^{+0.26}_{-0.25}$ |
| 2042 | 130.4 | $3.48^{+1.28}_{-0.94}$ | $3.68^{+1.26}_{-0.92}$ | $1.29^{+0.33}_{-0.32}$ |
| 2159 | 102.8 | $2.96^{+0.99}_{-0.74}$ | $3.48^{+0.96}_{-0.77}$ | $1.96^{+0.37}_{-0.35}$ |
| 2310 | 199.9 | $2.42^{+0.64}_{-0.50}$ | $2.79^{+0.62}_{-0.51}$ | $1.87^{+0.29}_{-0.28}$ |
| 6153 | 837.4 | $0.99^{+0.17}_{-0.14}$ | $1.21^{+0.17}_{-0.15}$ | $2.11^{+0.23}_{-0.21}$ |

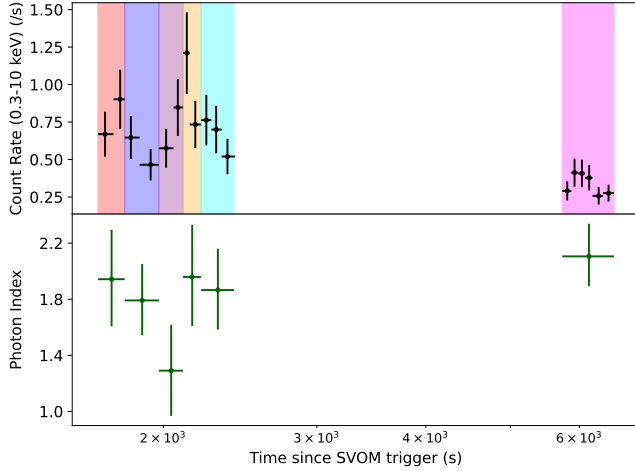


Figure B1. Top: XRT count rate lightcurve of the three flaring episodes, where the highlighted sections indicate the six $\text{SNR} = 5$ spectral bins. The late-time XRT data at ~ 3.35 d does not meet the SNR threshold and so is not included in the spectral analysis. Bottom: evolution of the best-fit photon index with time.

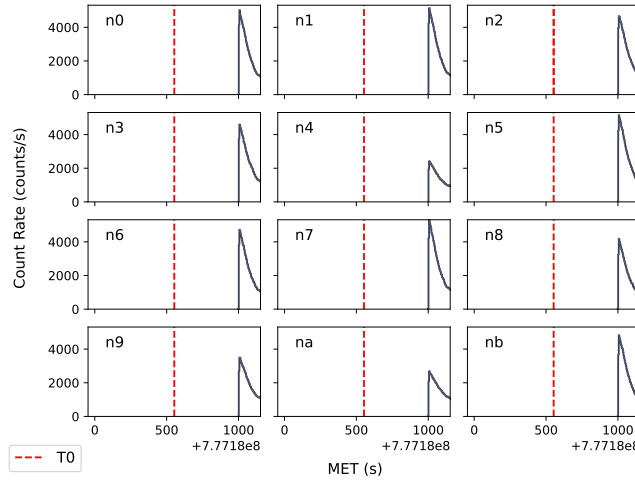


Figure B2. Light curves of all NaI detectors on *Fermi*/GBM between $T_0 - 600$ s and $T_0 + 600$ s (where T_0 is the *SVOM* trigger time, indicated by the dashed red line). The lack of counts around T_0 is due to *Fermi* being over the South Atlantic Anomaly.

APPENDIX B: SUPPLEMENTARY FIGURES

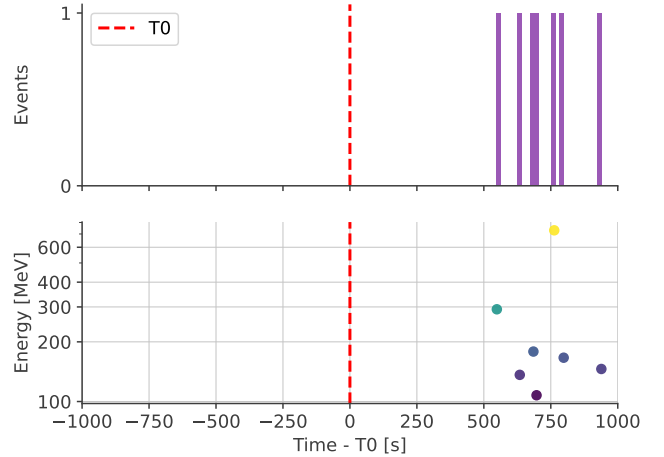


Figure B3. *Fermi*/LAT event data between $T_0 - 600$ s and $T_0 + 600$ s (where T_0 is the *SVOM* trigger time, indicated by the red dashed line). Top: number of events detected by the LAT. Bottom: energy of detected events. The lack of counts around T_0 is due to *Fermi* being over the South Atlantic Anomaly.

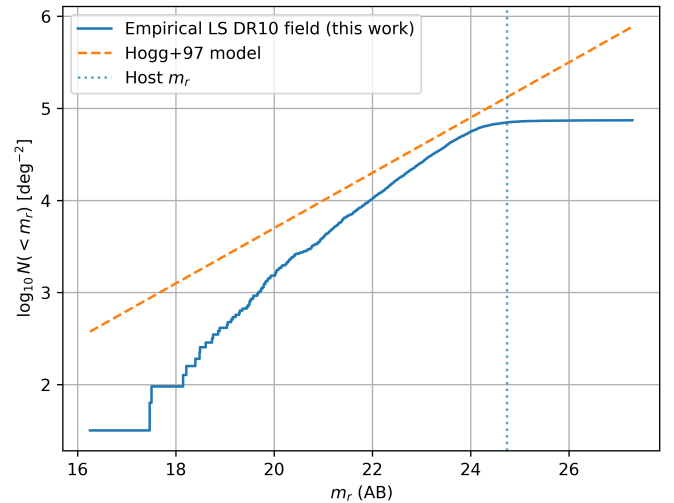


Figure B4. Cumulative galaxy counts in LS DR10 around GRB 250818B, measured within a 0.1° cone and restricted to galaxy-like, unmasked sources with significant r -band flux (type $\in \{\text{REX}, \text{EXP}, \text{DEV}, \text{SER}\}$, $\text{allmask_g} = \text{allmask_r} = \text{allmask_z} = 0$, $\text{flux_r} > 0$, $\text{flux_ivar_r} > 0$; blue step curve). The dashed line shows a simple Hogg et al. (1997) R -band number–counts model for comparison. The empirical counts follow a similar slope in $\log_{10} N(< m_r)$ versus m_r but with a lower normalisation by a factor of ~ 2 , likely due to our strict selection and the limited field size. The dotted vertical line marks the host-galaxy magnitude used to estimate $\sigma(< m_r)$ for the chance-coincidence calculation.

AFFILIATIONS

- ¹School of Physics & Astronomy, Monash University, Clayton VIC 3800, Australia
- ²Astrophysics Research Institute, Liverpool John Moores University, 146 Brownlow Hill, Liverpool L3 5RF, UK
- ³Department of Physics, University of Warwick, Gibbet Hill Road, Coventry CV4 7AL, UK
- ⁴School of Physics and Astronomy, University of Birmingham, Edgbaston, Birmingham, B15 2TT, UK
- ⁵Institute for Gravitational Wave Astronomy, University of Birmingham, Birmingham, B15 2TT, UK

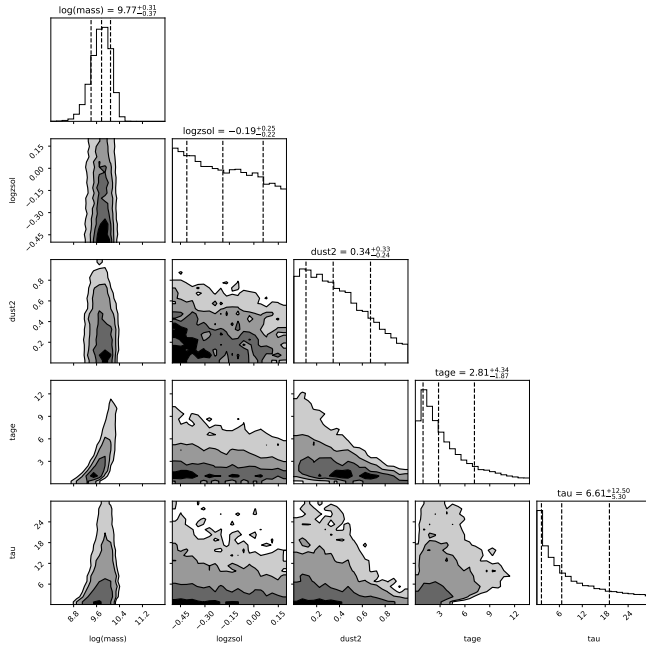


Figure B5. PROSPECTOR corner plot for the fitted parameters in the parametric delayed- τ model (e.g. stellar mass, metallicity, attenuation, population age, and τ). Shown for completeness; see Fig. 12 for the physically interpreted subset.

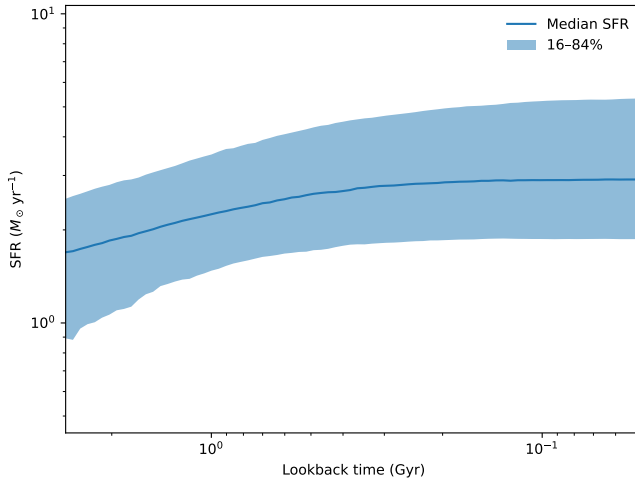


Figure B6. Star-formation history implied by the parametric delayed- τ PROSPECTOR fit: posterior median SFR as a function of lookback time (solid line), with the 16–84% credible interval (shaded). With the current photometric baseline, the recent SFR is weakly constrained; deeper blue/UV and NIR photometry would tighten the SFH constraints.

⁶Department of Astronomy, Cornell University, Ithaca, NY 14853, USA

⁷School of Physics and Astronomy, University of Leicester, University Road, Leicester, LE1 7RH, UK

⁸Department of Physics and Astronomy, Northwestern University, Evanston, IL 60208, USA

⁹Center for Interdisciplinary Exploration and Research in Astrophysics (CIERA), Northwestern University, Evanston, IL 60208, USA

¹⁰National Research University ‘Higher School of Economics’, Fac-

ulty of Physics, Myasnitskaya ul. 20, Moscow 101000, Russia

¹¹Space Research Institute of the Russian Academy of Sciences (IKI), Profsoyuznaya ul. 84/32, Moscow 117997, Russia

¹²Radio Astronomy and Geodynamics Department of Crimean Astrophysical Observatory, 298688 Katsiveli, Crimea

¹³Institute of Astronomy of the Russian Academy of Sciences, Moscow, Russia

¹⁴Astrophysics Research Cluster, School of Mathematical and Physical Sciences, University of Sheffield, Sheffield, S3 7RH, UK

¹⁵Research Software Engineering, University of Sheffield, Sheffield, S1 4DP, UK

¹⁶Instituto de Astrofísica de Canarias, E-38205 La Laguna, Tenerife, Spain

¹⁷Armagh Observatory & Planetarium, College Hill, Armagh, BT61 9DG, Northern Ireland, UK

¹⁸National Astronomical Research Institute of Thailand (NARIT), 260 Moo 4, T. Donkaew, A. Maerim, Chiangmai 50180, Thailand

¹⁹Department of Physics & Astronomy, University of Turku, Vesilinnantie 5, Turku, FI-20014, Finland

²⁰Jodrell Bank Centre for Astrophysics, Department of Physics and Astronomy, The University of Manchester, Manchester, M13 9PL, UK

²¹Institute of Cosmology and Gravitation, University of Portsmouth, Portsmouth, PO1 3FX, UK

²²Departamento de Astrofísica, Univ. de La Laguna, E-38206 La Laguna, Tenerife, Spain

²³Department of Astrophysics/IMAPP, Radboud University, 6525 AJ Nijmegen, The Netherlands

²⁴Institute of Astronomy and Kavli Institute for Cosmology, University of Cambridge, Madingley Road, Cambridge CB3 0HA, UK

²⁵School of Physics, University College Cork, Cork, T12 K8AF, Ireland

²⁶School of Sciences, European University Cyprus, Diogenes Street, Engomi, 1516 Nicosia, Cyprus

²⁷Centre for Astrophysics Research, University of Hertfordshire, College Lane, Hatfield, AL10 9AB, UK